CORE
Metadata, citation and similar papers at core.ac.uk
Provided by University of Wisconsin-Milwaukee

University of Wisconsin Milwaukee
UWM Digital Commons

Theses and Dissertations

May 2016

Monitoring Cellular Metabolism with Near-infrared Spectroscopy

Jeffrey Jay Sugar
University of Wisconsin-Milwaukee

Follow this and additional works at: https://dc.uwm.edu/etd


Part of the Electrical and Electronics Commons

Recommended Citation
Sugar, Jeffrey Jay, "Monitoring Cellular Metabolism with Near-infrared Spectroscopy" (2016). *Theses and Dissertations*. 1209.
https://dc.uwm.edu/etd/1209

This Thesis is brought to you for free and open access by UWM Digital Commons. It has been accepted for inclusion in Theses and Dissertations by an authorized administrator of UWM Digital Commons. For more information, please contact open-access@uwm.edu.

MONITORING CELLULAR METABOLISM WITH NEAR-INFRARED SPECTROSCOPY

by

Jeffrey Sugar

A Thesis Submitted in

Partial Fulfillment of the

Requirements for the Degree of

Master of Science

in Engineering

at

The University of Wisconsin-Milwaukee

May 2016

ABSTRACT

MONITORING CELLULAR METABOLISM WITH NEAR-INFRARED SPECTROSCOPY

by

Jeffrey Jay Sugar

The University of Wisconsin-Milwaukee, 2016
Under the Supervision of Professor Mahsa Ranji

Aims: Although NIRS oximetry has been widely used in clinical and research settings to monitor oxygen consumption in muscles (1), it is not necessarily able to obtain cellular metabolic levels directly. Oxygen saturation will only change with aerobic metabolism (2); however, anaerobic metabolism cannot be assessed by monitoring oxygen saturation. This work aims to measure cell oxygenation and blood oxygenation, simultaneously, by applying oximetry to hemoglobin/deoxyhemoglobin and to cytochrome c oxidase (CCOX). A custom build NIRS device called the cytoximeter was constructed to achieve this goal. This work could have important impacts on monitoring neurological diseases, Postural Tachycardia Syndrome (POTS), and epilepsy.

Introduction: CCOX is the terminal enzyme in the electron transport chain (ETC) and as such will be responsive in changes in either aerobic or anaerobic metabolism (3). CCOX transports a number of electrons over a single cycle of the ETC. As the enzyme accepts electrons, it enters a reduced state. Monitoring the redox state of CCOX in a given tissue will reflect the amount of metabolic activity in that tissue (9). We developed a novel device that monitors the changes in optical densities of a tissue. Using Beer's law and the difference in absorption spectra of reduced and oxidized CCOX, it is possible to measure the relative changes in concentration of these chemicals (4).

Methods: In order to observe and separate the CCOX signals from absorption changes due to whole blood changes, a six wavelength absorption spectroscopy device is constructed. This device uses the optimal source detector separations, obtained by numerical photon migration simulations, for monitoring superficial muscles and cortical brain tissue. In order to validate the device performance, several phantom studies are conducted followed by clinical investigations. In the clinical setting, the device was applied to the gastrocnemius muscles of patients undergoing a tilt table test during a standard of care neurological examination.

Results: The phantom studies showed that the device was able to obtain changes in the concentration and the redox state of CCOX in a medium with optical properties similar to the tissues found in the calf and skull. When applied in a clinical setting, the device produced reproducible and predictable results. The clinical results are partially verified by the use of a commercially available oximeter, which validates the changes in hemoglobin and oxy hemoglobin obtained by our custom-made cytoximeter.

Conclusion: This work is a novel approach to the non-invasive monitoring of CCOX simultaneously with blood oxygen saturation by use of NIR spectroscopy. While there is currently no gold standard with which to compare these results to, the ability to separate cellular metabolism in the presence of large changes in blood volume during a clinical procedure is a promising first step toward clinically monitoring the energy expenditure of tissues. Further work is underway to correlate changes in CCOX redox state to the level muscular exertion. This will allow the researchers to quantitatively monitor CCOX redox changes during different levels of exercise.

To my mother, father, and brothers

All of whose accomplishments serve as inspiration to me

TABLE OF CONTENTS

LIST OF FIGURES

LIST OF TABLES

LIST OF ABBREVIATIONS

CHW	Children's Hospital of Wisconsin
CCOX	Cytochrome C Oxidase
CW	Continuous Wave
DAQ	Data Acquisition
ETC	Electron Transport Chain
IACUC	Institutional Animal Care and Use Committee
IRB	Institutional Review Board
Hb	Hemoglobin
HbO_2	Oxyhemoglobin
LED	Light Emitting Diode
MCW	Medical College of Wisconsin
POTS	Postural Orthostatic Tachycardia Syndrome
O_2 Sat	Oxygen Saturation
SNR	Signal to Noise Ratio
SVD	Singular Value Decomposition
VI	Virtual Instrument

ACKNOWLEDGEMENTS

Firstly, I must thank my graduate advisor Dr. Mahsa Ranji for her help and support during my graduate studies. I would not have been able to accomplish this work without her guidance and commitment to excellence. I am truly grateful for the opportunity to work in the Biophotonics Lab during the past three years.

I must also express my gratitude to the staff of the Medical College of Wisconsin who were instrumental in the progress of this progress. I must thank Dr. Harry Whelan for his expertise and enthusiasm. Dr. Whelan was also instrumental in promoting my research and connecting me with the professionals at MCW who made the clinical testing possible. I am also grateful for Dr. Brenden Quirk for supplying the bio-chemical knowledge necessary for this work and for spending hours acquiring and purifying the chemicals used in this research. I should also thank Drs. Thom and Gizela Chelimsky, who graciously provided access to their clinic and helped to recruit the subjects used in this study.

I am also grateful to all the members of the Biophotonics Lab past and present. I am grateful to Whitney Linz and Erfan Masoudi for their instrumental role in laying the ground work for the device used in this study. I am also indebted to Zahra Ghanian and Dr. Mette La Cour for inconveniencing them with constant reviews and input in my Thesis and Presentation.

Thank you all.

Chapter 1 Introduction

1.1 My Contributions

I have developed a cytoximeter probe based on an existing oximetry device in the bio photonics lab as a new clinically relevant device. I have also implemented a signal processing algorithms which performed new functions in the device. This new version of the oximeter has the capability to monitor cytochrome c oxidase (CCOX) redox levels with the goal of non-invasively assessing the metabolic rate of muscles. This ability could provide crucial diagnostic information by giving more information than is available from a traditional blood oximetry device. The ability to detect metabolism independent of blood oxygenation could help determine parameters of disease, quantitatively. For example, in a syndrome such as Postural Tachycardia Syndrome (POTS) this marker could measure the patients' ability to maintain muscle tone. This device has been used to collect data in a clinical setting at the Children's Hospital of Wisconsin (CHW). I have prepared an Institutional Review Board (IRB) approved protocol for additional testing of subjects at UWM. The new study aims to correlate the CCOX redox state for muscle force.

In order to make the new probe, I had to implement several novel approaches to oximetry in the new device. Firstly, I built a probe with 6 different light sources with different wavelengths. This greater number of wavelengths required a more advanced data processing protocol and filtering algorithm. The device also required a more robust data processing technique, which could avoid the common pitfalls that caused erroneous results in more complex spectroscopy applications.

In the course of this project, several different programming languages were used. The device is s driven by a laptop running a LabVIEW Virtual Instrument (VI). The VI is responsible

for driving the light sources on the device and recording and displaying data in real time. The VI saves the data for offline processing for higher fidelity data.

Offline data processing techniques were written in MATLAB. These techniques were new to this cytoximeter device and were required for the extraction of the CCOX signal. MATLAB was also utilized to generate figures for presentations involving this work.

I have also written a C++ program that utilizes a well-known Monte Carlo simulation algorithm so we could easily simulate different imaging conditions to try and optimize our design to target tissue at certain depths. These simulations informed our choice of source-detector separations.

As a further method of verification of the device, I have designed a new testing protocol that is currently being applied at UWM. This protocol aims to correlate the amount of force a subject exerts to the redox state of CCOX. This correlation required the construction of a new testing apparatus to measure the force that a subject can apply with their foot. I have also been the primary contact for this protocol, recruiting subjects and ensuring compliance with the IRB.

I am certified by the Institutional Animal Care and Use Committee (IACUC), to perform heart extraction Langendorff procedures. Although this has not been my main project, I have contributed significantly to heart fluorometry experiments. This has led to me being obliquely involved in several other projects in the Biophotonics Lab.

1.2 Biological Background

1.2.1 Cellular Respiration and Metabolism

One of the most widely used and beneficial applications of near infrared spectroscopy (NIRS) is to monitor the health and function of a biological tissue both noninvasively and non-destructively. For instance, the health of a tissue during a surgical procedure can be monitored

and maintained by ensuring that the tissue is supplied with enough blood and oxygen (1). The function of muscles can be monitored by observing the amount of oxygen that the muscle is absorbing (2). This work aimed to add another marker to observe the function of the tissue. While monitoring oxygen consumption shows that the tissue is undergoing aerobic cellular respiration, it does not supply any information about anaerobic cellular metabolism. By undergoing anaerobic cellular metabolism and not consuming oxygen, the muscle may appear to have a low metabolic demand when in-fact the rate of metabolism is high and the tissue is simply predisposed to anaerobic metabolism (3).

1.2.2 Oxyhemoglobin and Deoxyhemoglobin

Aerobic metabolism requires both oxygen and glucose to function. The oxygen that fuels the aerobic metabolism comes from oxygen molecules dissociated from the oxyhemoglobin (HBO_2). Upon losing its oxygen molecules, the HBO_2 undergoes a minor change in shape and becomes Deoxyhemoglobin (HB), sometimes simply referred to as hemoglobin. The hemoglobin is re-oxygenated in the pulmonary system where there are high serum levels of O_2 (4). By monitoring local levels of O_2 saturation (the ratio of HBO_2 to whole blood), it is possible to infer to what extent the tissues are undergoing aerobic metabolism (5, 6).

1.2.3 Cytochrome C Oxidase and Redox State

Although monitoring hemoglobin is widely used in both clinical and academic settings (5, 7-9), it does not fully show the metabolic nature of the tissue because it does not take into account the anaerobic metabolism. Anaerobic metabolism requires only glucose as fuel and will not affect the O_2 saturation immediately (10). This is why monitoring CCOX redox state would provide valuable information.

CCOX is the terminal receptor in the electron transport chain (ETC). This chain is critical to producing the electrochemical gradient that provides the energy to create ATP (11, 12). When the CCOX molecule accepts electrons at the end of the ETC, it enters a reduced state. When CCOX oxidizes, it uses the energy produced to pump protons across the cell membrane. Although this process is extremely quick, it is comparatively slow considering the speed at which the entire ETC process runs. This has the effect of more reduced CCOX in response to an increase in metabolism (11). CCOX will perform this function regardless of if it is in aerobic or anaerobic metabolism (12). Therefore, one would expect a more reduced state during either form of metabolism.

1.2.4 POTS

Postural orthostatic tachycardia syndrome (POTS) is a fairly common disease, affecting half a million Americans annually, with a poorly understood pathophysiology(13). It is classified as a collection of symptoms, which may arise from several different path physiologies (13, 14). The primary symptom that defines POTS is persistent and chronic tachycardia shortly after assuming a standing position. The symptom will generally improve when the person sits or assumes a prone position (14). Because assuming an upright position elicits a response of tachycardia in healthy patients in order to qualify as a symptom of pots the tachycardia must persist for five to thirty minutes and not be accompanied by hypotension, decrease in blood pressure (15). The persistence of this tachycardia causes a number of secondary symptoms such as lightheadedness, fatigue, headache and mental malaise (15). These symptoms are often severe enough to lead to a high level of functional disability (16).

POTS is a heterogeneous disorder with several different underlying conditions causing the tachycardia response to orthostatic changes. For intervening therapies to be maximally effective, it will be important to understand the cause and mechanisms of a patient's symptoms (13). Further complicating the issue, the symptoms can also be caused by other conditions such as deconditioning from extended bedrest (17). The primary difference between POTS and these other conditions is that the tachycardia in POTS persists even after the natural orthostatic hypotension has been corrected. This seems to suggest that at least some POTS patients suffer from an exaggerated response to a decrease in blood pressure. There are many proposed causes for this decrease ranging from autoimmune diseases to pathophysiological brain malfunctions (14, 15, 18). To show how monitoring cytochrome c oxidase could be used to advance the understanding of POTS, two of these potential causes will be discussed here. These two conditions are an overreaction of the sympathetic nervous system and an inability to maintain muscle tone (19).

When a person stands or adopts another upright position, there is a shift of blood to the lower body. This will cause venous pooling in the legs. This pooling leads to a decrease of blood return to the heart. To make up for this lack of return, the body has two natural responses; the first is an increased heart rate. The second is an increased muscle tone in the extremities to help return blood to the heart. In normal situations, the heart rate will be an immediate response to the drop in blood pressure and the muscle tone will eventually take over and heart rate will decrease (18). However, in some patients with a specific cause for POTS, the muscle tone is not maintained and the tachycardia will persist.

In other POTS patients, the tachycardia will persist because of a hyper adrenergic state (11, 12). This state leads to an increase of the sympathetic nervous responses. Among these

responses are increased blood pressure and dilation of veins. This kind of POTS is commonly accompanied by anxiety and chronic fatigue disorders.

Monitoring when and where metabolism increases will not only help to diagnose which subset of POTS a patient suffers from, but also help to understand the mechanisms that lead to POTS. For instance, monitoring the metabolism of the calves in a heads up tilt table test could show if the muscles attempt to increase tone to maintain venous return, or if the symptoms are being caused by a hyper adrenergic response.

1.3 Basis of Near-Infrared Spectroscopy

1.3.1 Oximetry

A tissue oximeter uses absorption spectroscopy to monitor the amount of hemoglobin and HBO_2 present in the tissue. A light is shone on the tissue and the amount of light observed at the detector is measured and used to calculate the amount of light that has been absorbed in the tissue. Oximeters are generally one of the two different configurations, transmission or reflection (20). In transmission oximeters, the light and detector are placed on opposite sides of a thin tissue typically a finger or earlobe (21, 22). In reflective configurations, the light source and detectors are placed on the same side of the tissue and the light that is observed at the detector has been scattered back from the tissue (20).

Continuous wave oximeters use a light source that remains at a single wavelength for a given period of time. Continuous wave oximeters, rely on the modified Beer-Lambert law that relates the amount of light that has been absorbed to the length of the path that the light travels and the concentrations of chemicals that were in the tissue (23). The Beer Lambert law is as follows:

$$\Delta OD = -\log\left(\frac{I(t)}{I_o}\right) = \sum L_i \mu_{\lambda_i} \Delta C_i \quad (1.1)$$

Where $I(t)$ is the light observed at the detector, I_o is the expected or incident light at the detector, μ_i is the absorption coefficient of a given chemical, ΔC_i is the change in concentration of a given chemical and L is the average path length that the photon takes from the source to the detector. This equation is true for all wavelengths λ although the absorption coefficients will vary with wavelength according to the absorption spectra of chemical i (24). The process for determining the path length is discussed in the next section.

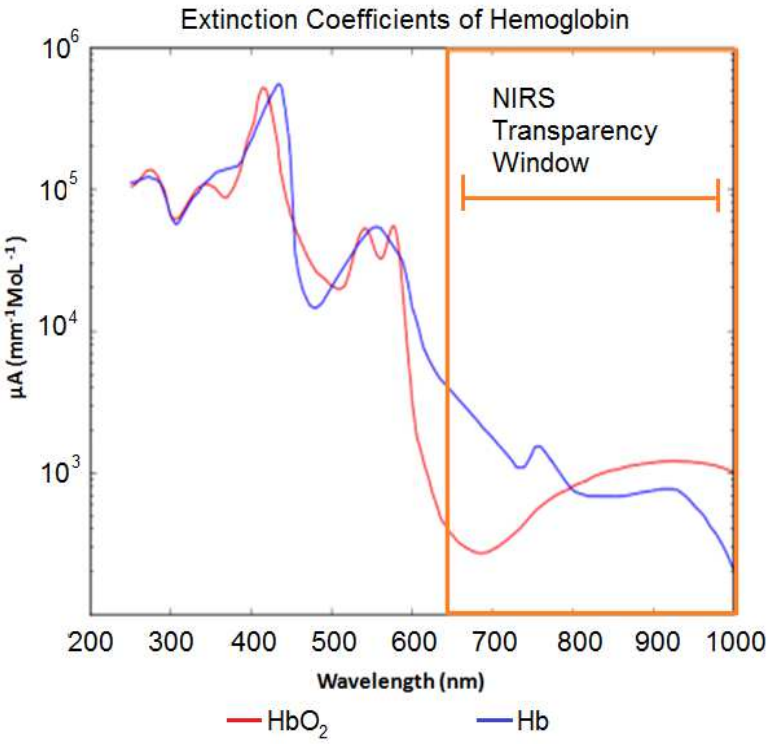

Figure 1.1 The absorption spectra for both the oxyhemoglobin (HbO_2) and deoxyhemoglobin (Hb). The highlighted region is the diagnostic window in NIR, which tissue has the lowest absorption and is nearly transparent to light.

When hemoglobin attaches or detaches from oxygen, it undergoes a slight conformational change that causes a slight difference in absorption spectra. A figure comparing the absorption spectra of Hb and HbO_2 is seen in figure 1.1. Tissue oximeters often use two different

wavelengths to determine the concentrations of both species of hemoglobin. Originally oximeters used red and green light, however today light wavelengths are generally chosen in the NIRS transparency window also highlighted in figure 1.1. These wavelengths are selected to give the highest signal to noise ratio (SNR). In order to do this, the oximeter typically uses wavelengths where the absorption spectra of the two species are very different (25). Occasionally, a third wavelength is added to the oximeter that corresponds to a point where the two wavelengths have very similar absorption coefficients (26). This cross point is known as the isobestic point and can be used to measure blood volume.

In previous versions of the device with only blood oximetry, the wavelengths selected have been 735nm, 805nm and 850nm. For the new set-up, only two wavelengths, 735nm and 850nm are needed to calculate the two species of hemoglobin present. The two wavelengths can be used to calculate the amount of hemoglobin and HBO_2 by solving the following systems of equations.

$$\Delta OD(735nm) = -\log\left(\frac{I(735nm)}{I_o(735nm)}\right) = L(\mu_{Hb}(735nm)\Delta C_{Hb} + \mu_{HbO2}(735nm)\Delta C_{HbO2}) \quad (1.2)$$

$$\Delta OD(850nm) = -\log\left(\frac{I(850nm)}{I_o(850nm)}\right) = L(\mu_{Hb}(850nm)\Delta C_{Hb} + \mu_{HbO2}(850nm)\Delta C_{HbO2}) \quad (1.3)$$

These can be solved with a simple regression equation:

$$\begin{pmatrix}\Delta OD_{735}\\ \Delta OD_{850}\end{pmatrix} = L\begin{pmatrix}\mu_{Hb}(735nm) & \mu_{HbO2}(735nm)\\ \mu_{Hb}(850nm) & \mu_{HbO2}(850nm)\end{pmatrix}\begin{pmatrix}\Delta C_{Hb}\\ \Delta C_{HbO2}\end{pmatrix} \quad (1.4)$$

The last equation can be used to monitor the blood volume with the following equation:

$$\Delta OD(850nm) = L(\mu_{Hb}(850nm)\Delta C_{Hb} + \mu_{HbO2}(850nm)\Delta C_{HbO2}) \quad (1.5)$$

1.3.2 Addition of Cytochrome C oxidase

A similar method used to track changes in HbO_2 and Hb can be extended to monitor CCOX by adding additional wavelengths to the detection device.

Like hemoglobin changes whether associated or dissociated with an oxygen molecule, CCOX undergoes a similar conformational change that affects its absorption spectra as the molecule reduces or oxidizes (27). Wavelengths must be chosen to give the most robust estimation of the amount of CCOX in the tissue. Similar to hemoglobin, a wavelength is chosen where reduced CCOX is more absorbing, another wavelength where the oxidized CCOX is more absorbing and a third wavelength where the two are very similarly absorbing. Figure (1.2) shows the absorption spectra for all four chemicals monitored in this study. The three wavelengths that were selected for monitoring CCOX are 600nm for reduced cytochrome, 620nm for the isobestic point where the two are similar and 650nm for the oxidized CCOX. Although each of the wavelengths is affected by each of the chromophores present each of the wavelengths in this system are primarily responsible for detecting one chromophore. 600 nm detects reduced CCOX, 650nm detects oxidized CCOX. The isobestic wavelength 620nm detects the entire amount of CCOX.

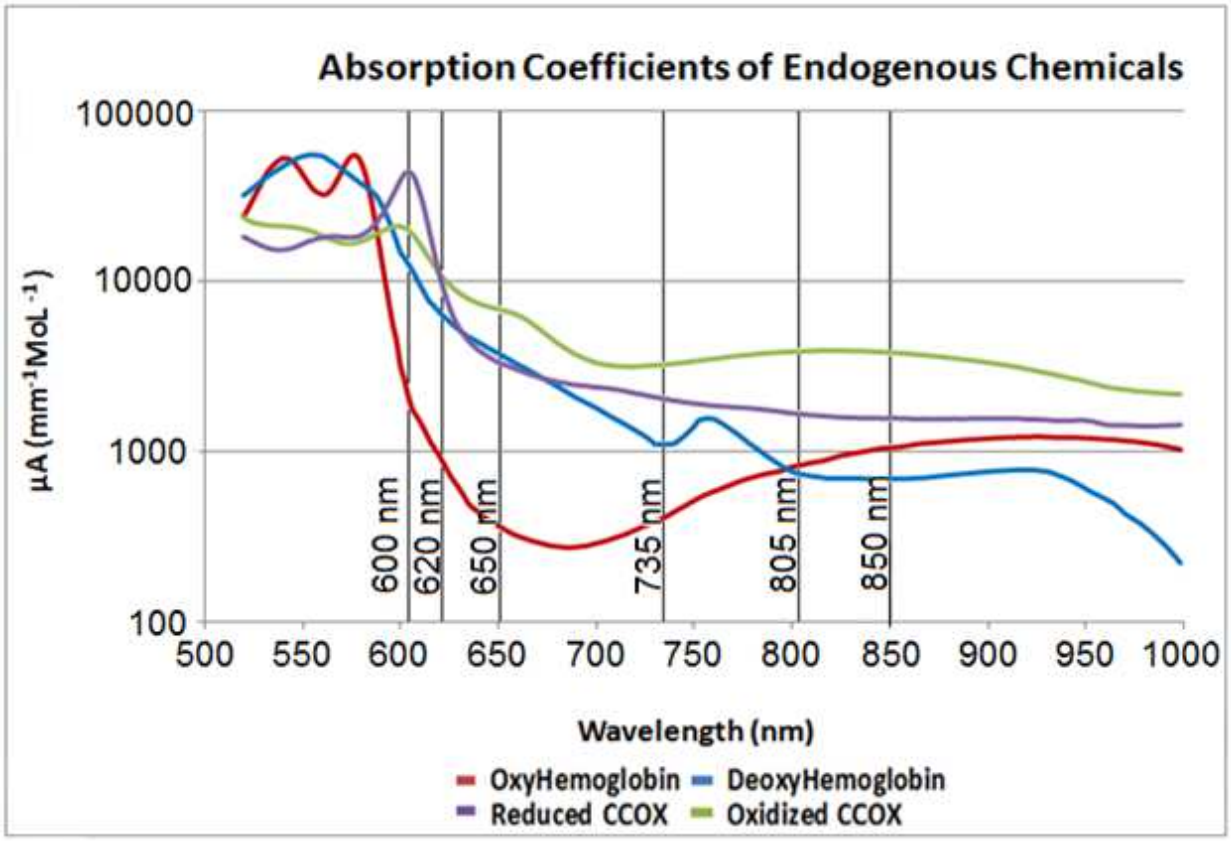

Figure 1.2 The absorption spectra of the four chromophores that will be detected in this work. The six wavelengths that are used to identify these chemicals are represented as black vertical lines across the spectra.

Unlike monitoring the hemoglobin, CCOX will not account for the majority of light absorption at any of these wavelengths, accounting for only up to 10% of the signal (11). Therefore, it is necessary to cancel out the effects of the hemoglobin on absorption before calculating the amount of cytochrome in the tissue. This is done by using all six wavelengths to find the concentrations of the four chemicals as noted in the figure. The following equation allows the extraction of concentration of these four parameters:

$$\begin{pmatrix} \Delta OD_{600} \\ \Delta OD_{620} \\ \Delta OD_{650} \\ \Delta OD_{735} \\ \Delta OD_{805} \\ \Delta OD_{850} \end{pmatrix} = L \begin{pmatrix} \mu_{Cyt\ ox}(600nm) & \mu_{Cyt\ red}(600nm) & \mu_{Hb}(600nm) & \mu_{HbO2}(600nm) \\ \mu_{Cyt\ ox}(620nm) & \mu_{Cyt\ red}(620nm) & \mu_{Hb}(620nm) & \mu_{HbO2}(620nm) \\ \mu_{Cyt\ ox}(650nm) & \mu_{Cyt\ red}(650nm) & \mu_{Hb}(650nm) & \mu_{HbO2}(650nm) \\ \mu_{Cyt\ ox}(735nm) & \mu_{Cyt\ red}(735nm) & \mu_{Hb}(735nm) & \mu_{HbO2}(735nm) \\ \mu_{Cyt\ ox}(805nm) & \mu_{Cyt\ red}(805nm) & \mu_{Hb}(805nm) & \mu_{HbO2}(805nm) \\ \mu_{Cyt\ ox}(850nm) & \mu_{Cyt\ red}(850nm) & \mu_{Hb}(850nm) & \mu_{HbO2}(850nm) \end{pmatrix} \begin{pmatrix} \Delta C_{Cyt\ ox} \\ \Delta C_{Cyt\ red} \\ \Delta C_{Hb} \\ \Delta C_{HbO2} \end{pmatrix} \quad (1.6)$$

This equation is in the form of an over constrained regression problem. This problem can be solved by application of a Penrose pseudo-inverse to each side of the equation to be left with an estimate of the concentrations of the absorbing species on the right hand side of the equation. While this method would work under ideal conditions, in practice there are several numerical problems often arise from approaching a problem such as this.

In an over constrained regression problem, more data is collected than is needed to calculate the explanatory variables. This means that often times the concentrations found do not fully account for the total absorption in the tissue. Some extra absorption is included in the tissue. This extra absorption is the residual. This problem may tempt some designers to use four wavelengths of light for the four absorbers and frame the problem as an exactly constrained regression problem, however, there is literature support that using an over constrained regression model is more accurate, mainly due to the fact that there are more than four absorbers present in the tissue and the presence of new wavelengths serves to cancel out the effects of other absorbers (28-30).

Also by taking six wavelengths instead of four, some co-linearity is introduced into the regression matrix. This makes the estimation of the absorbers present in the tissue more susceptible to noise. These problems, as well as an approach for correction methods, will be discussed in greater depth in chapter 3.

1.4 Tissue Optics

The oximeter works by applying a continuous wave (CW) light source to a tissue to record change in the absorption across the path of photons from the source to the detector (23). This path must be determined to find the depth of penetration and the fluency of light at the point where each detector is located. This problem can be modeled mathematically by using the radiation transfer equation,

$$\frac{\partial I(\bar{r},\bar{s})}{\partial s} = -\varepsilon_{eff} I(\bar{r},\bar{s}) + \frac{u_{s,eff}}{4\pi} \int 4\pi I(\bar{r},\bar{s}')\rho\,(\bar{s},\bar{s}')d\Omega', \tag{1.7}$$

where $\partial I(\bar{r},\bar{s})$ is the radiance, ε_{eff} is the effective molar extinction coefficient, $u_{s,eff}$ is the effective scattering coefficient, $\rho(\bar{s},\bar{s}')$ is the scattering phase function, and $d\Omega'$ is the unit solid angle about $\bar{s}'$ (31, 32). However, this equation is only solvable analytically under a very limited set of assumptions and numerical methods often need to be employed. The problem is further compounded by the fact that boundary conditions must be applied to each of the layers of the biological tissue (31-33).

The problem can be simplified by assuming that the reduced scattering coefficient is much greater than the absorption coefficient (32). The reduced scattering coefficient is given by:

$$\mu'_s = \mu(1-g) \tag{1.8}$$

where g is the anisotropy factor. Under this assumption one can apply diffusion theory by assuming that the shape of the photon path is primarily affected by the scattering and changes in

absorption and do not affect the shape of the light propagation. This assumption holds true for many biological tissues including epidermis, dermis, muscle and even skull (34, 35).

The assumption that the light propagation problem in the tissues can be modeled by the diffusion equation is essential to the methods used in oximetry. Under the diffusion equation assumption, changes in concentrations of absorbing chemicals, which impact primarily the absorption of the tissue, will not greatly affect path length and depth of penetration of photons in the tissue. This allows the modified Beer Lambert Law equations to consider a constant path length L, even with blood concentrations changing in the tissue, because the optical properties of the tissue will not drastically change over time (6, 23, 36).

1.5 Monte Carlo Simulations

As an alternative to using the transfer equation, which treats the light as a continuous wave problem, the equation can be thought of as the summation of photon particles undergoing random scattering and absorption events. Under this formulation of the problem, one can employ a Monte Carlo simulation to model the path of the photons. Monte Carlo is a stochastic method that models the path of electrons through a tissue by repeatedly simulating the flight of a packet of photons through the tissue (37, 38).

Modeling photon propagation with a Monte-Carlo simulation is a well-researched practice that has been largely unchanged since the 1990's (39, 40). The popularity of the method has led to several freely available Monte Carlo simulations to be available (41). While these are the standard for Monte Carlo simulations, they have quite high processing times.

We implemented a smaller scale Monte Carlo simulation to perform initial analysis of different source and detector geometries.

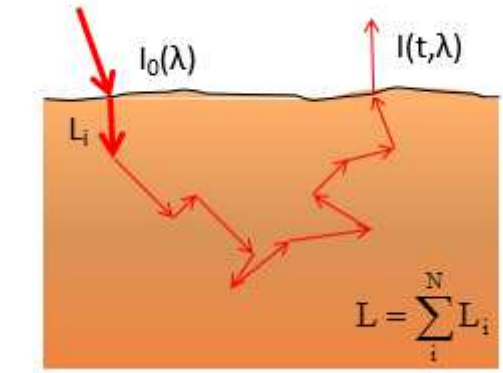

Figure 1.3 A single photon path through the tissue. After being scattered multiple times the photon leaves at the same plane it was injected from. The path length L_i is the path length of photon i; the total path length L is the average of all these photon paths.

A Monte Carlo simulation models the random walk of photons as they propagate through the tissue. A single photon will undergo several scattering events in its trip from the source to the detector. If a photon reaches the detector it will have crossed the plane that it was injected into and the path has curved back upon itself producing a "banana shaped path". A single photon's path through a tissue sample can be seen in figure 1.3. Photons also have the potential to have their path terminating in the tissue by being absorbed; these effects must be taken into account by the Monte Carlo simulation. By repeating this process, the two important factors can be obtained, the average depth of penetration and the average path length.

The Monte Carlo algorithm will be discussed briefly here. Firstly, a photon packet is inserted into the tissue with a weight representing the amount of photons left in the packet. The first step of the Monte Carlo process is the determination of step size. This step size represents how far the photon will fly before the next iteration. This step size is a random variable related to the mean free path (39). The step size is generated by the following equation:

$$\Delta s = \frac{-\ln(\xi)}{\mu_t} = \frac{-\ln(\xi)}{\mu_s + \mu_a} \tag{1.9}$$

Where ξ is a random variable uniformly distributed between zero and one. The photon will then fly the step distance, where it will undergo absorption and attenuation. Attenuation will reduce the weight of the photon packet according to the ratio of the μ_a to the sum of μ_a and μ_s. The photon is scattered by changing the direction it is facing and will head during the next step phase. The angle that is formed by the photon's original path and its scattered path is determined by the anisotropy factor g. The anisotropy factor varies from zero to 1. The closer anisotropy factor is to 1, the less the average angle between the original and scattered angle (38). The photon packet will then proceed at this direction for another step and would be scattered and attenuated at that location. This process is repeated until the photon packet either leaves the tissue or is attenuated past a certain threshold. This algorithm is illustrated in the flow chart in figure (1.4).

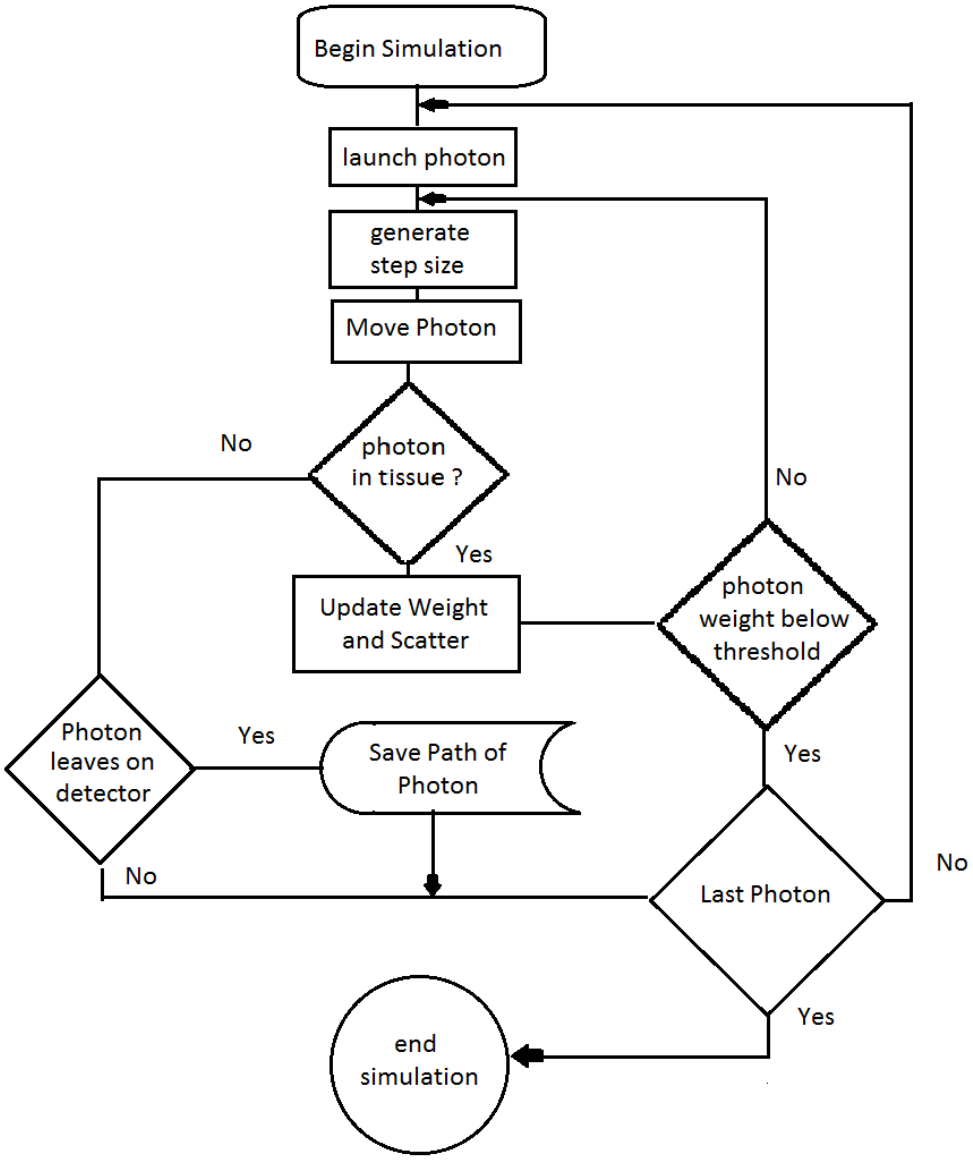

Figure 1.4 Flow Chart of the Monte Carlo Simulation for generating the paths of photons from the led source to the detectors. The sum of all paths that exit on the detector are saved and used to generate the photon paths. Paths that exit elsewhere are not considered in the Monte Carlo Simulation.

The paths of all photons that exit at the detector are saved and averaged. To this classic algorithm a small addition was added to decrease the processing time. Assuming that the tissue is radially symmetric any photons that exit the tissue at a certain radius away from the source could

be considered to reach the detector. Any path that did terminate in this radius was rotated so that every path exits at the same point before being saved. This was found to greatly increase the speed of the Monte Carlo simulations by increasing the percentage of photons that would reach the detectors.

This algorithm is used to generate four different Monte Carlo simulations. Two simulations are performed on forehead-brain geometry and two on calf muscle geometry. On both geometries, simulations are performed at two and three centimeter source detector separations. The optical properties of these different tissues are reported in table (1). In general, it is very difficult to obtain accurate measurements for anisotropic factors for tissues and it is generally assumed that most tissues are forward scattering with g ≈ 0.9 (34, 35, 42).

Tissue	Absorption Coefficient mm^{-1}	Scattering Coefficient mm^{-1}
Dermis	0.02	23
Sub Dermis	0.011	1.2
Muscle	0.05	9
Skull	0.020	30
Brain	0.048	10

Table 1.1 Table showing the optical properties used for conducting Monte Carlo simulations to determine the effective depth of penetration of each detector. These are not meant to be authoritative as inter-subject variability will cause the values to vary widely.

The simulation was written in a C++ environment, and image processing is performed with MATLAB.

The Monte Carlo simulations are run on multi-layered geometries. One geometry represents the tissue present in the calf. The skin is modeled by 0.3 mm of dermis, 1 mm of sub dermis and a semi-infinite layer of muscle beyond. The results of these simulations are displayed in figure 1.5.

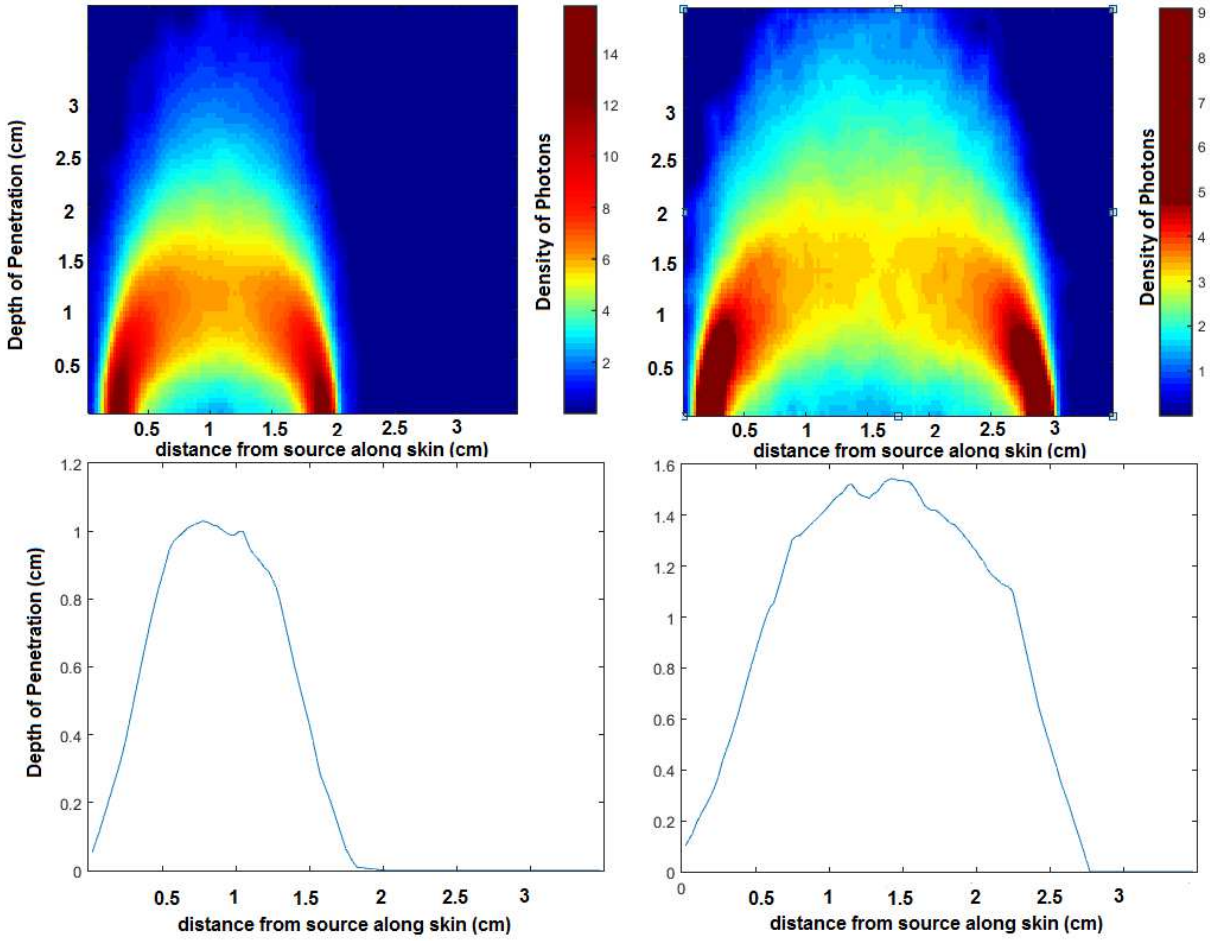

Figure 1.5 Results of Monte Carlo simulations for skin and muscle geometries at both 2 cm and 3cm source detector separations. The densest parts of these simulations are shown on the bottom row to give a sense of the average penetration of these optical paths.

A second set of simulations are run on a geometry simulating the tissue in the forehead. This geometry is modeled by 0.3 mm of dermis 1 mm of sub dermis, 4 mm of skull and then a semi-infinite layer of brain (43). The results of these simulations are displayed in figure 1.6.

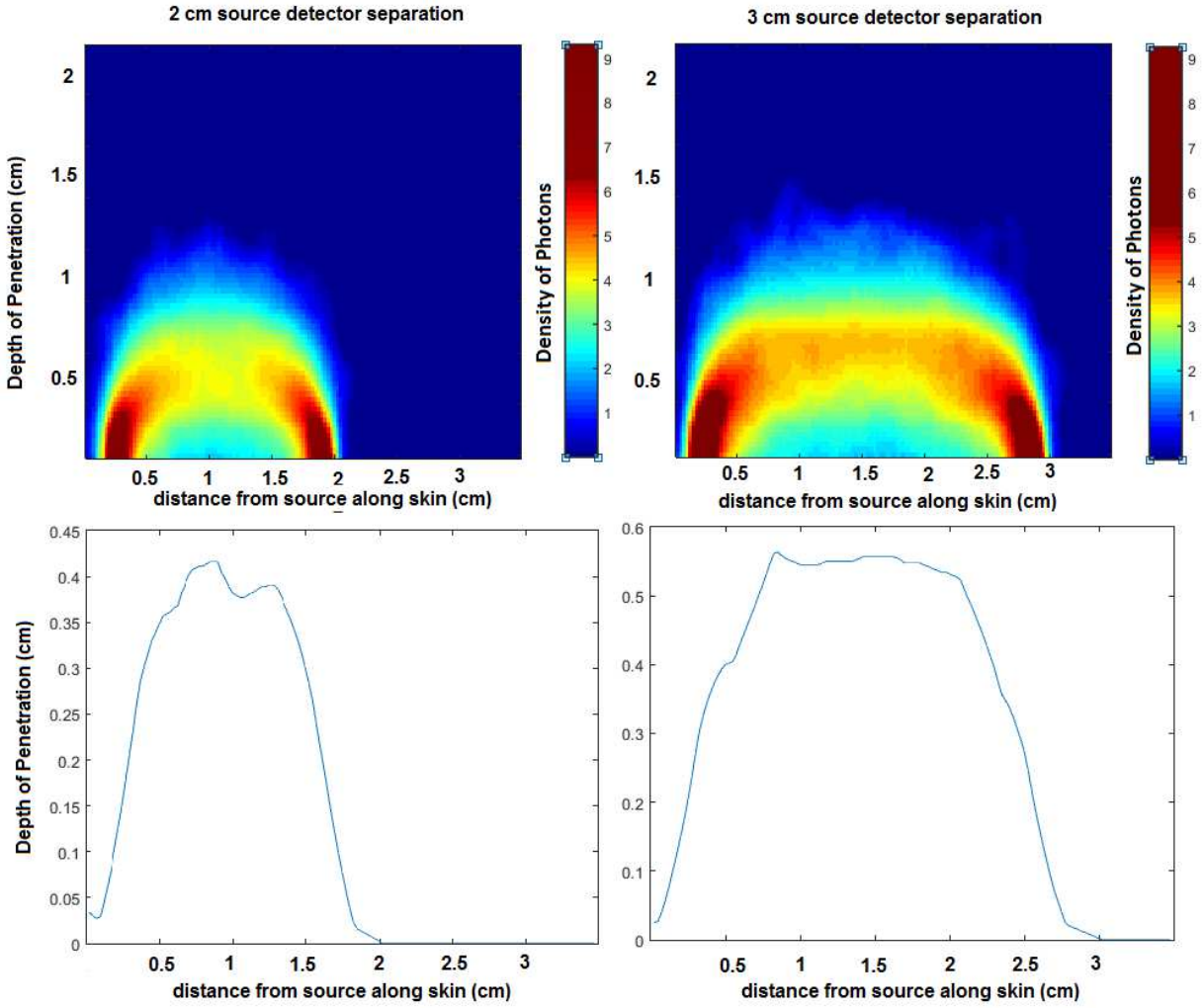

Figure 1.6 Results of Monte Carlo simulations for skin, brain and skull geometries at both 2 cm and 3cm source detector separations. The densest parts of these simulations are shown on the bottom row to give a sense of the average penetration of these optical paths. The optical penetration is greatly decreased with respect to the muscle geometry because of the high scattering coefficient of the skull.

Chapter 2: Instrumentation and Design

As discussed in Chapter 1, the primary goal of this study was to use NIRS to identify the chromophore cytochrome c oxidase (CCOX) molecule. CCOX served as a marker of the amount of metabolic activity in the tissues. This chapter contains the details on the device I made to achieve these goals.

A previous blood oximeter probe had been designed to observe the blood volume and oxygen saturation in superficial muscle. The cytoximeter probe was designed to perform oximetry and CCOX readings, simultaneously. The new probe has two source detector separations to allow the device to monitor tissues' different depths. This probe was designed with the goal of being versatile so that it could be applied to superficial muscles, deeper muscles and skull. The first clinical data acquired in the gastrocnemius muscle during a heads up tilt table test performed by clinicians at the Children's Hospital of Wisconsin (CHW). During the test, a commercially available oximeter was used in conjunction with our probe as a method of verifying our results. Figure 2.1 shows the placement of both of these devices during these tilt table examinations. In the following sections, I explain the hardware, software protocols, and verifications of the cytoximeter.

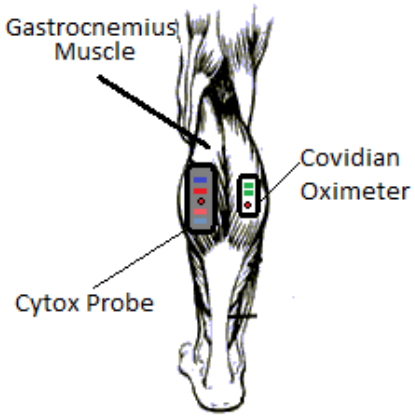

Figure 2.1 positions of the two probes during the heads up tilt table test

2.1 Hardware implementation

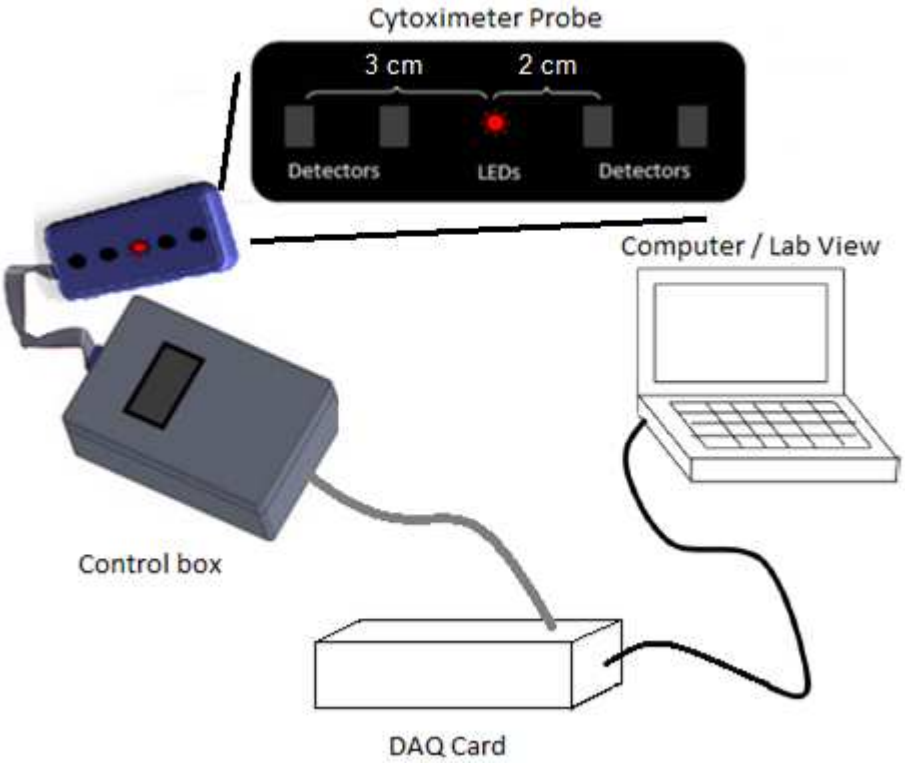

Figure 2.2 Configuration of the hardware setup of the cytoximeter.. This probe was connected via a VGA cable to the Control box. The Control box conditions the signal from the probe, and drives the LEDs. The Control box communicated with the laptop that is recording the data throughout the experiment.

A schematic of the cytoximeter setup can be seen in Figure 2.2. The device had two components, which were custom made for this project, a probe and a control box. The probe contained the light sources and detectors that are used to measure the optical densities of the tissue. The control box contained amplifiers for the detectors, and turned the LEDs on and off in sequence. The data was acquired by the DAQ board and recorded by the laptop. The laptop also displayed the results of the CCOX and hemoglobin data in real time. The main data processing was done in post processing in a process that will be discussed in chapter three.

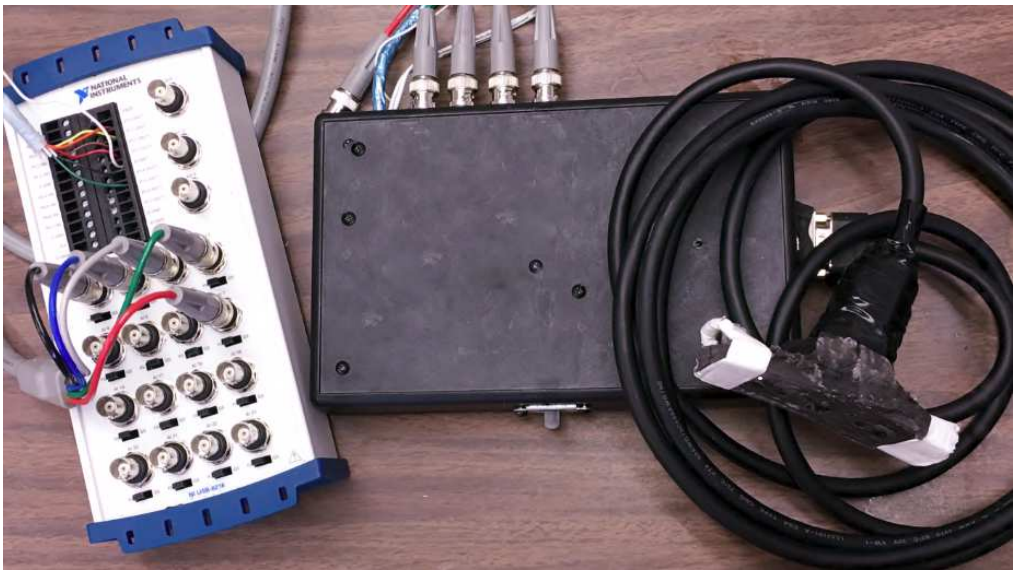

Figure 2.3 The DAQ board control box and probe of the oximetry hardware

This section contains information on the two custom built pieces of equipment, the control box and the probe. The probe refers to the head of the device that was placed upon the subject's muscle surface. The box controls this probe optoelectronically. This system is called the cytoximeter, displayed in figure 2.3

2.1.1 Probe

The probe is capable of producing and detecting six separate wavelengths of light. The light came from 4 different LED's. One LED was the triple wavelength LED that was used in the first and second generation of the device. This LED is capable of creating three wavelengths (Epitex, L735/805/850/PD-35B32, Kyoto, Japan). The remaining three wavelengths were each provided by a single 3 mm LED. (ROHM semiconductor, 650nm 3.2mm LED, ROHM semiconductor, 620nm, 3.2mm LED, and ROHM semiconductor, 605nm, 3.2mm LED). Each LED had a plastic Fresnel lens clipped over it. These lenses helped to create a more collimated

and point-like source for light injection. Four multi-pixel photon counters (MPPC's) (Hamamatsu, S1133-14, Kyoto, Japan) were used as detectors in the probe. These detectors were organized in two pairs to provide two different depths of penetration. The first pair of detectors were placed at a source detector separation of 2 cm. The second pair of detectors were placed at a distance of 3 cm. As discussed in the previous chapter the different source detector separations produced different depths of penetration of the light.

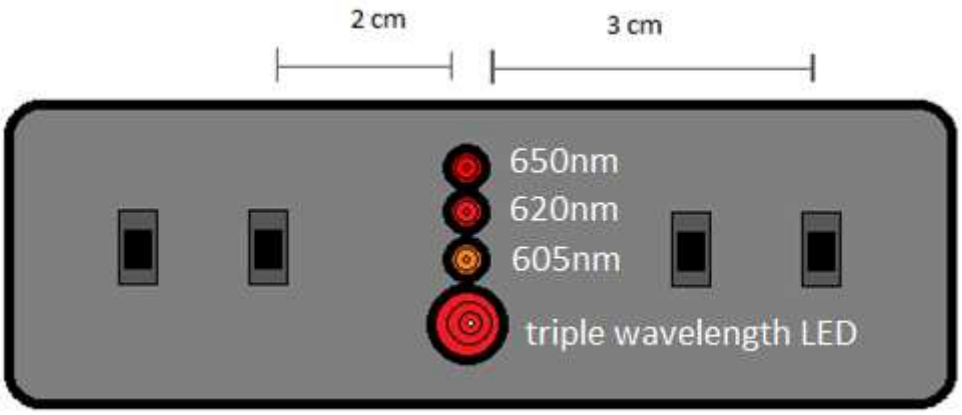

Figure 2.4 The probe head geometry. The Cytoximeter consist of four LEDs arranged in a line to ensure that the distance from each of the sources to each detector in a pair is the same. Two detectors are arranged at a separation of 2 cm to give a depth of penetration of 1 cm, two detectors are arranged at 3 cm to give a depth of penetration of 1.5 cm.

As seen in figure 2.4, the detectors and light sources were arranged in two perpendicular lines. Because we could not find a readily available way to include all six wavelengths on a single LED, this geometry was used to minimize the difference in path length between each source and each detector in one of the pairs. In this geometry of sources and detectors each 2cm detector was the same distance from the 605nm source. The 2cm detectors were also the same distance from the 650nm source. However the distance from the 605nm and 650nm source detector separations were not the same. The source detector configuration shape was kept by a 16-gauge steel wire. This addition was found to be essential because the probe was long and

required a certain level of deformation to make a good contact with the skin of the patient. These factors added stress to the components and would cause the wires connecting the components to break and lose their electrical contact with the components. The components and wire frame were embedded in a molded silicon Rubber (Rebound ®) dyed with black India Ink. Staining the probe was important to block light pollution and reflection from the probe. The probe is connected via a VGA cable to the control box. The VGA cable was used both for high fidelity of signal and robustness of the probe.

2.1.2 Control Box

The control box contained the amplifiers for the signal that came from the detectors on the probe. It also contained the drivers for LED's. The control box communicated with the DAQ board on both the analog and digital channels of the DAQ board. The LED's were turned on and off by transistors in common emitter mode in the control box. These transistors were controlled by the digital output from the DAQ board. In previous versions of the control box the sequence of LEDs was controlled by a digital oscillator and counting circuit. This circuit was removed because the previous strategy used a different analog channel for each of the wavelengths. In this version of the control box, the signals from the different wavelengths are timeshared along one analog channel. This new method reduced the number of channels needed from 24 to 4. Therefore, a less expensive DAQ-board could be used. However, it did require lowering the sampling rate to compensate for the response time of the analog channel.

2.2 Software Implementation

Several new pieces of software were designed and implemented for use in the cytoximeter. This section will provide details for the Lab VIEW program that runs the experiment.

2.2.1 LabVIEW

The software that operates the DAQ board and control box in the experiment was a LabVIEW virtual instrument (VI). The VI accepted four analog input channels from the DAQ board, one from each of the detectors, and output a single eight-bit digital number to control which LED was on.

The DAQ board was programmed to continuously sample each of the channels at a rate of 5kHz. The lights were switched at a variable rate of up to 20Hz. This translates to a range of samples per wavelength and sampling rate for an entire 6 wavelengths cycle. For example, the quickest sampling rate the system was capable of was 3.33 Hz for a six wavelengths cycle with 250 samples at each wavelength. This allowed for an update of the estimate of CCOX and hemoglobin value, 3 times per second.

The entire program was made up of a number of sub-VIs that each performed a function that was necessary to the data analysis process. All of these VIs saved their data in a Technical Data Management Stream (TDMS) file for further processing. The following sections discuss each of these sub-VIs. Each of these sub-VIs was accessed through a top level hub VI that also controlled the names and paths of the files generated by each sub VI

2.2.2 Dark Current Correction

The first VI in the series was the dark current correction VI. This VI obtained the amount of signal that was due to dark current on each of the channels. Dark current is a small voltage that arises in an optoelectronic system even when no light is being seen by the detectors. Dark current arises in every optoelectronic system and is caused by leakage current of the semiconductors in the detectors and by parasitic interactions with other components in the system. This source of noise was measured and corrected by placing the probe on a black surface so that the only

voltage read by the VI is from dark current. This test was conducted while the LED's were being switched on to factor in the parasitic effects.

This procedure was originally performed before each test, however our protocol made it untenable to do this test before every single tilt table experiment so, one dark current test would be done in the morning before testing each day. The dark current values were observed to be stable over a long time, and over multiple tests. Therefore, it was assured that small changes in dark current were a minimal source of error in the system. Because this process was not repeated before each of the experiments each time, subsequent VIs use the most recently obtained dark current values. A screen shot of this VI in function is included in figure 2.5.

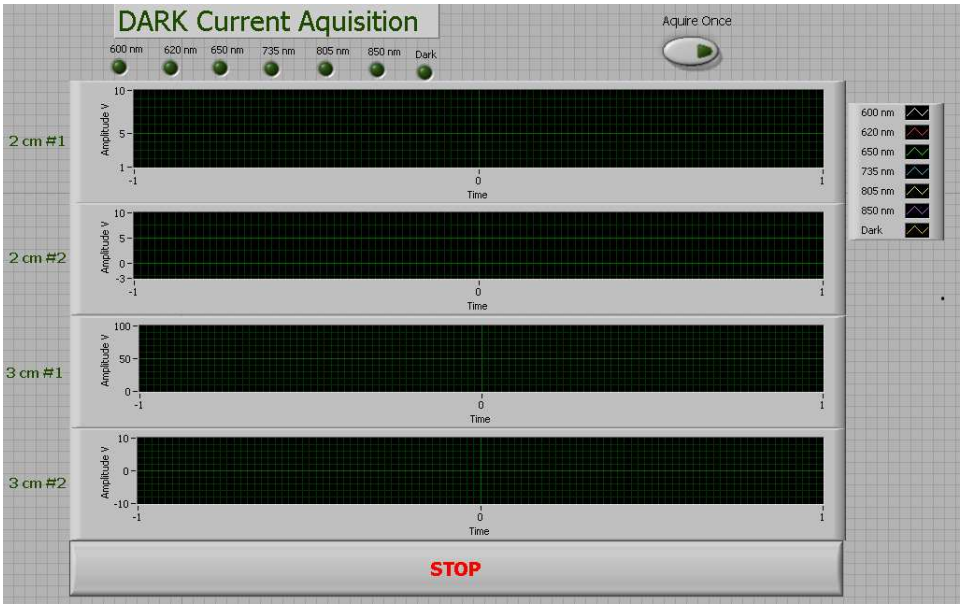

Figure 2.5 Screen Shot of the Dark current acquisition VI. This VI was responsible for removing the effects of leakage current and parasitic effects from the experiments.

2.2.3 Ambient Pollution Correction

Even though the detectors were located on the underside of the probe when it was applied to the skin the detectors were sensitive enough to pick up the ambient light in a room with bright lighting. Since the probe was designed for clinical use, it was assumed that the lighting conditions in the room couldn't always be kept dark. To correct for this ambient light pollution, a second sub VI measured light seen by the probe after it had been applied to the subject's leg. The LED's were not flashed during this procedure so that only the ambient light was recorded during this time.

Several repetitions of this procedure led to the conclusion that this ambient signal, though small, varies from experiment to experiment and should be corrected for in each experimental procedure. It also appeared that the ambient light would vary from subject to subject, and even if the subject were to perform a second test a short while after completing the first. Like the process of acquiring dark current, this VI saved the ambient light intensities for future use. Because this process was repeated before each experimental procedure, the VI could save the ambient light levels as a variable that was used by later VIs.

2.2.4 Baseline Acquisition

In order to obtain optical densities, a baseline had to be established. The third VI obtains the baseline, during a period where the LEDs are turned on but the subject was not exercising or doing anything else to perturb the Hemoglobin or CCOX readings. This was done until the baseline measurements were stable for at least a minute. These light measurements were used as the incident light in the calculations for determining the optical densities. We did not want to have light from sources other than our LEDs affecting this baseline, so the dark current and

ambient light had to be subtracted from the light levels seen during this step to produce a baseline.

This VI saved the incident light levels, after they had been stable for a period of time, for use in the next VI. The VI also saved the logs as a TDMS file but this file was not used in post processing and was only used when determining what went wrong if an experiment yielded very unexpected results. This VI is displayed in figure 2.6.

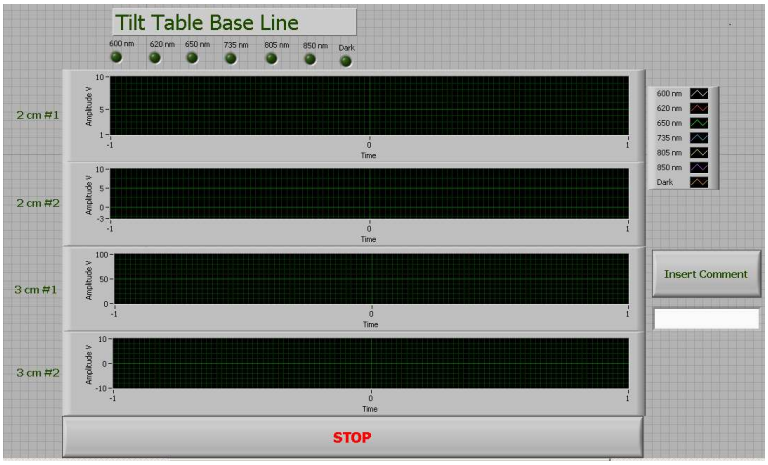

Figure 2.6 screen shot of Baseline VI

2.2.5 Acquisition VI

The last VI was the primary VI running while the experiment is being performed. This VI was responsible for reading the light levels from the probe and converting these values into OD changes. It used the OD values to estimate the changes in hemoglobin and CCOX values. The VI reported these estimates to the user in real time during the experiment. The VI performed these functions by subtracting the dark current and ambient light from the light levels obtained and then applying the modified Beer Lambert law.

I also gave the user the ability to make comments while the experiment was running. This allowed the user to make observations that were time stamped and saved along with the data that has been collected. This was added because several times there were interruptions in the tilt table

process, such as the subject fainting or the tilt being delayed so the administers could attend to the subject. The VI can be seen in figure 2.7.

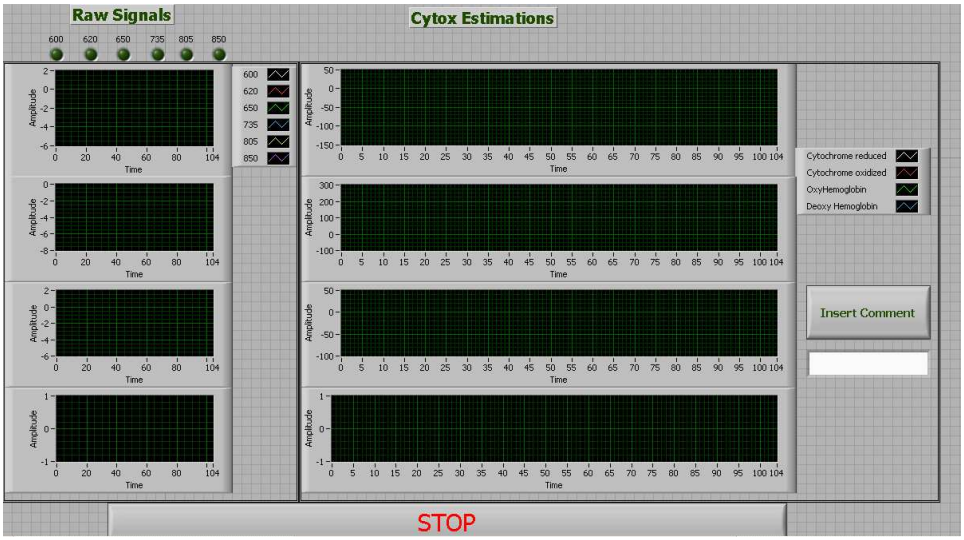

Figure 2.7 Snapshot of the Acquisition VI which is used to collect data during the Tilt and report real time estimations of CCOX and Hemoglobin Values. The user of this VI could record observations that mark what happened during the experiment.

2.2.6 Top Level VI

The VIs described in the previous sections needed to be performed in a specific order to obtain the changes in CCOX and hemodynamic signals. This order was controlled by a top level VI that transferred the data between each of these VIs. The protocol that the program followed is presented as a flow chart in figure 2.8.

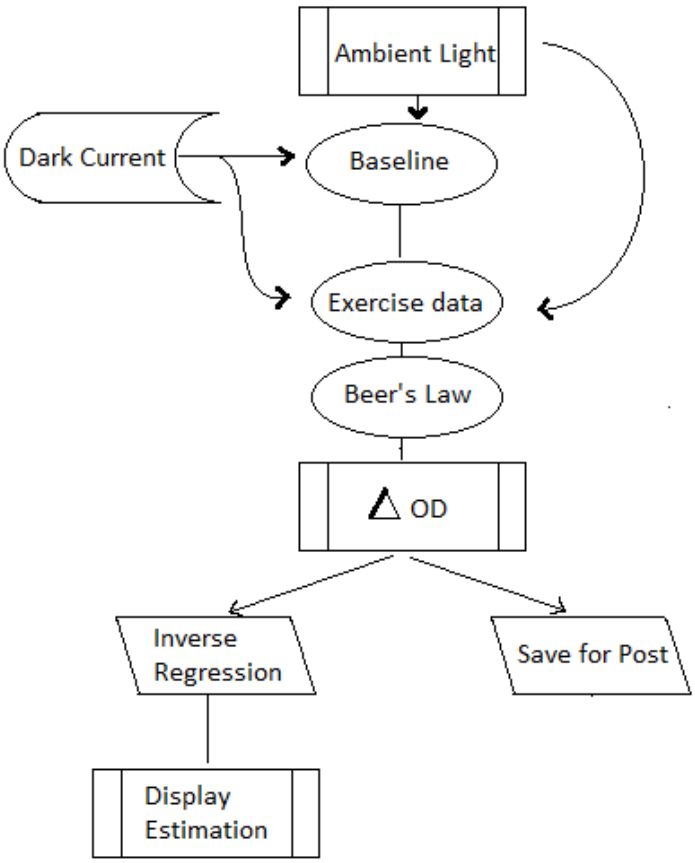

Figure 2.8 Flow chart of the processes used during a single experiment involving the Cytoximeter. As Discussed before the dark current correction could not be performed each time and instead the most recently performed dark current experiment will be used to correct for dark current. The ambient light correction was performed every time. The next step was performing a baseline. The last step was to use the acquisition VI to obtain optical densities and display the estimates of CCOX and hemodynamic changes.

2.2.7 Offline Data Analysis

The data from each of the VIs is saved as a TDMS file. These files were converted into an excel spreadsheet by the TDMS reader plugin in excel. This excel spreadsheet was read by a custom written MATLAB code. This code analyzed the information by performing a data analysis technique known as Kalman filtering, which is discussed in the next chapter (put in page number later). After this Kalman filtering algorithm was completed, estimates of the trends of HBO_2, HB, Oxidized CCOX, and Reduced CCOX are produced. In addition to these four

signals, other three signals were also calculated, blood volume, oxygen saturation (O_2 Sat) and redox state.

Ideally O_2 sat would represent the ratio of HbO_2 to whole blood, Blood Volume would report the total blood in the tissue and redox state would represent the ratio of reduced CCOX to total CCOX. However, since the device can only detect relative changes in each of the four chemicals and not absolute amounts, this is not possible. Instead the O_2 sat, blood volume, and redox State were estimated from the following equations. These were approximations that tell about the general trend of the O_2 Sat, CCOX Redox State and Blood volume.

$$\Delta O_2 Sat = \Delta Oxyhemoglobin - \Delta DeoxyHemoglobin \quad (2.1)$$

$$\Delta BloodVolume = \Delta Oxyhemoglobin + \Delta DeoxyHemoglobin \quad (2.2)$$

$$\Delta Redox\ State = \Delta Reduced\ Cytox - \Delta Oxidized\ Cytox \quad (2.3)$$

The Matlab code generated figures for each of these signals. If comments were included in the Data acquisition VI, they were marked with a red vertical line in these figures.

2.3 Future Protocol

In order to correlate the results of this probe to muscle force exertion, I have designed and have had approved a new testing protocol that can be performed at UWM. This Protocol aimed to correlate the changes in the CCOX to muscle exercise in non-POTS affected subjects. This information can be used for statistical analysis with the data from POTS patients at MCW. In order to achieve these goals, I have designed and built a new foot force measuring apparatus using a six axis strain-gauge.

2.3.1 Strain Gauge

A six-axis strain gauge (Advanced Mechanical Technology, Inc., MC3A-1000, Watertown, MA) was used in the new protocol to measure the force that a subject applied with their foot. The strain gauge is seen in figure 2.9. The strain gauge has been used in previous studies involving oximetry when the Biophotonics Lab was studying the difference in healthy muscles and those affected by stroke. As such no new hardware had to be built or purchased to accommodate this strain gauge.

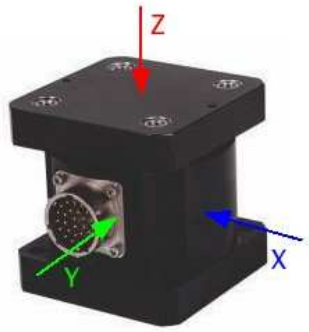

Figure 2.9 The strain gauge that will be used in the continuation of this project. The arrows indicate the default coordinate system. This image is a modified version of one from (44)

For this apparatus, I used the same amplifier and settings that were used by the previous designers of this device. The strain gauge is connected to an amplifier (custom-made, Hand Rehabilitation Lab, University of Wisconsin - Milwaukee), which was connected to the same DAQ board that was described in the previous sections. The gains on the strain gauge amplifier were set to 5,000 mv/mv for channels 1-3, and 1,000 mv/mv for channels 4-6.

2.3.2 Foot Restraint Apparatus

The new protocol required the ability to obtain the force that subjects were able to exert by flexing their foot while in standing, prone and sitting postures. This made the use of strain gauge

a challenging matter because the apparatus had to be able to be used in all these configurations. A custom built apparatus was constructed to hold the strain gauge in all these configurations. This apparatus can be seen in figure 2.10. The device was constructed from machined metal parts and lumber. The new device also included a foot restraint that is commercially available for use in rowing exercise machines (concept 2 model D).

Figure 2.10 The Foot restraint apparatus. This apparatus is designed to hold the strain gauge upright and on any side while allowing the subjects foot to access to the strain gauge.

2.4 Phantom Validation Experiments

Before any clinical trials were performed, a phantom was constructed in order to show it was possible to detect the presence of CCOX in an environment that mimicked *in vivo* optical properties. This section describes the methods used in the construction of such a phantom and the process of using the phantom to assess the function of the probe. There were two kinds of phantom that were used in this study. The first one was a solid phantom that was used to assess if the light had significant intensity to penetrate the tissues in question. The second kind of phantom used in this project was a two phase phantom that included a solid layer representing the upper tissues and a liquid layer representing sub dermal tissue.

2.4.1 Solid phantom

The solid phantom was created by using a one percent by mass agarose-gel (45) . Within this gel, two other products were suspended. which were used to alter the optical properties of the gel. The first product was intralipid, a fatty emulsion used as a nutrient delivery vehicle in hospitals. The fat in the emulsion contributed to the scattering coefficient of the gel with good reliability (46). The other product that was suspended in the gel is black India Ink. This ink was used to mimic the absorbing properties of various tissues (47). The ink does have a non-negligible contribution to scattering of the phantom so in order to construct a more reliable phantom, concentrations of both intralipid and India Ink were extrapolated from literature that used a phantom that contained both (45, 48). Particularly useful were the trends reported by Cubeddu et al (45). The data from these trends were used to create several layers of phantom that were responsible for the different layers of tissue.

The concentrations of Intralipid and India Ink added to the phantom, depended on the tissues the phantom was simulating. The optical properties of the tissues modeled in the phantoms and the amount of ink and Intralipid used to simulate those tissues are reported in table 2.1. The literature data that these are based on are reported in (45).

Tissue	Reduced scattering coefficient (mm^{-1})	Concentration of intralipid (% emulsion)	Absorption Coefficient (mm^{-1})	Concentration of India Ink by (% by volume)10^{-5}
Dermis	23	3.2	0.02	3.6
Muscle	9.0	1.1	0.05	8.2
Skull	30	4.3	0.02	3.6
Brain	10	1.25	0.05	8.2

Table 2.1 optical properties of the phantom and simulated tissues. The amount of ink was used to mimic absorption of tissue, and Intralipid was used to mimic scattering.

In order to construct the phantom, the agarose was mixed with water and heated in a microwave until the solution became entirely clear. After the solution cooled but before it started to solidify, the India Ink and Intralipid were added to the solution. The solution was put in a mold to cool. This process could be done several times to create a layered phantom as seen in figure 2.11

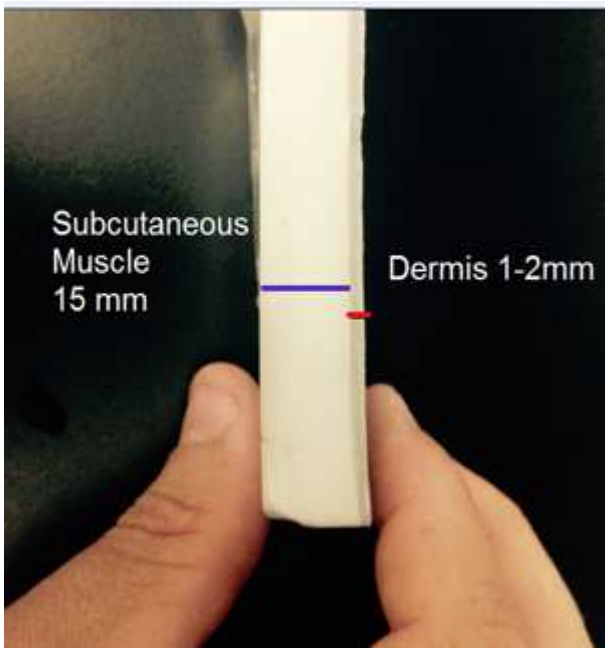

Figure 2.11 This phantom was created to simulate the optical properties of the calf with the same dermis and subcutaneous muscle dimensions that would be encountered in an in-vivo setting. Each layer of this phantom was created using an agarose gel with Intralipid and India Ink added to create the optical properties of a forearm tissue.

This solid phantom was used in the early stages of creating the device to ensure that the lights could adequately penetrate the tissue and ensure that the photodetectors were sensitive enough to detect light that has been attenuated by the tissue. Our tests showed that the photodetectors did have the ability to detect the levels of light being applied to the phantom.

2.4.2 Two Phase Phantom

The second phantom was made to ensure that the device was able to detect changes in CCOX concentrations in tissues that were below skin level. In order to do this a series of phantoms were used that had both a solid layer representing the superficial tissues and liquid layer beneath which represented the tissue of interest. These phantoms were constructed within a plastic cell culture flask (VWR cell culture flasks, Standard Line). An agarose gel layer was embedded on one side of the flask while the remaining volume of the flask is left empty. The rest of the flask was filled with a DI water, Intralipid and India Ink solution that mimicked the deeper tissues optical properties. The two phase phantom is shown in figure 2.12.

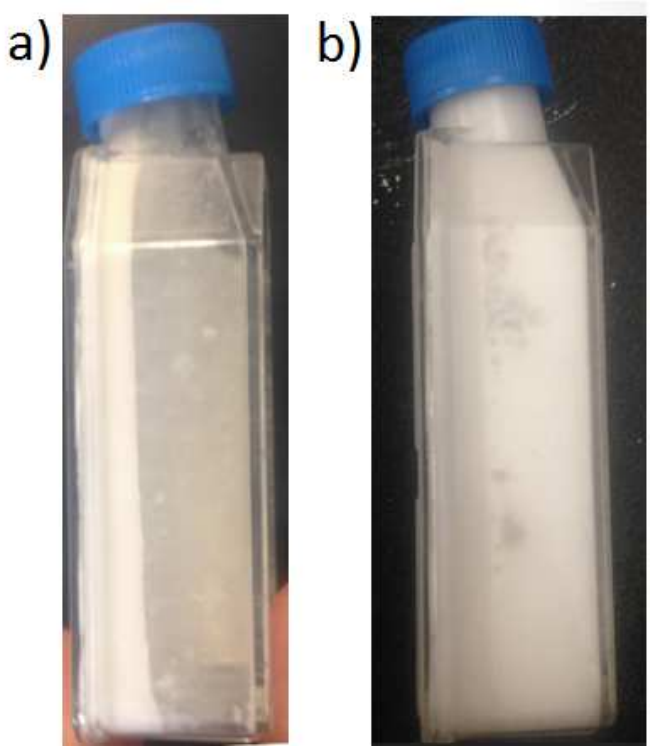

Figure 2.12 Steps in construction of a two phase phantom. Figure a) shows only the solid phase of the phantom which when dry is embedded into the cell culture flask and will not fall if the flask is turned on its side. Figure b) shows a phantom filled with the liquid phase.

Two of these two phase phantoms were created, one corresponding to the situation in which we would apply the probe to a superficial muscle and one corresponding to a situation in which the probe is applied to the skull.

2.4.3 Phantom Experiments

The two phase phantoms were used to test the performance of the probe at detecting changes in concentration of CCOX. In order to test this, the probe was applied to the side of the phantom that has the solid phase of the phantom. The probe was used to obtain data from the phantom. Oxidized CCOX was added to the solution in a series of boluses to produce changes in concentration in the phantom. As expected, the addition of CCOX to the phantom led to increases in the oxidized CCOX levels read by the cytoximeter. Opening the phantom caused disturbances in the liquid and may have let small amounts of air into the system. Therefore, each time a bolus of dithionite was added the system there was a large noisy signal added to the test. Even with this unavoidable noisy addition process, there still exists a clear trend in the amount of oxidized CCOX measured with the addition of each bolus. These results are presented in figure 2.13.

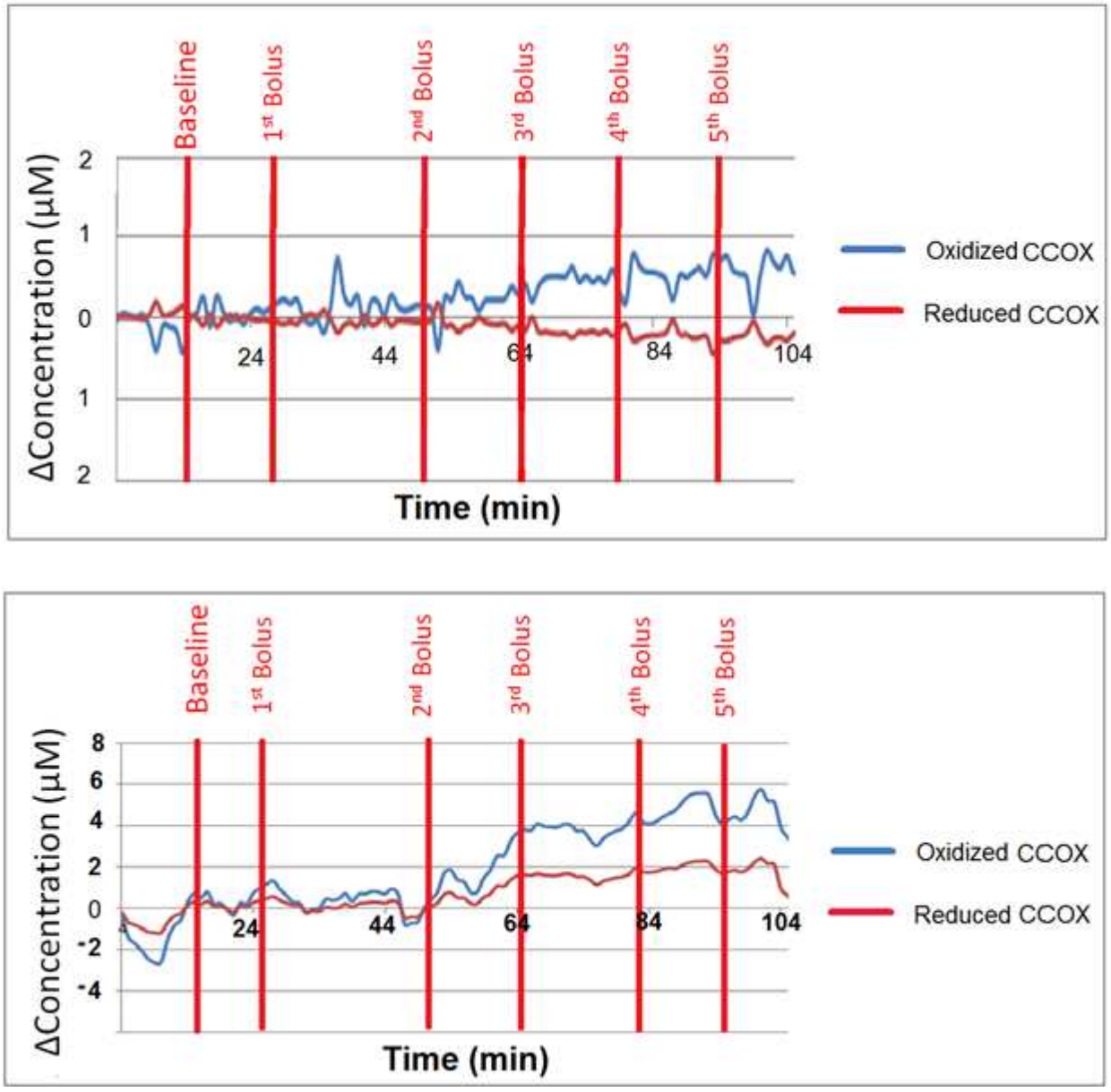

Figure 2.13 These graphs represent the progressive addition cytochrome oxidase to the phantom. Each bolus introduced causes an increase in the Oxidized CCOX. The experiment is performed on both a phantom representing the skull and brain geometry (top) and a phantom representing a calf geometry with dermis and superficial muscle layers (bottom).

The results of the Phantom experiments led to the linearity curves presented in figure (2.14).

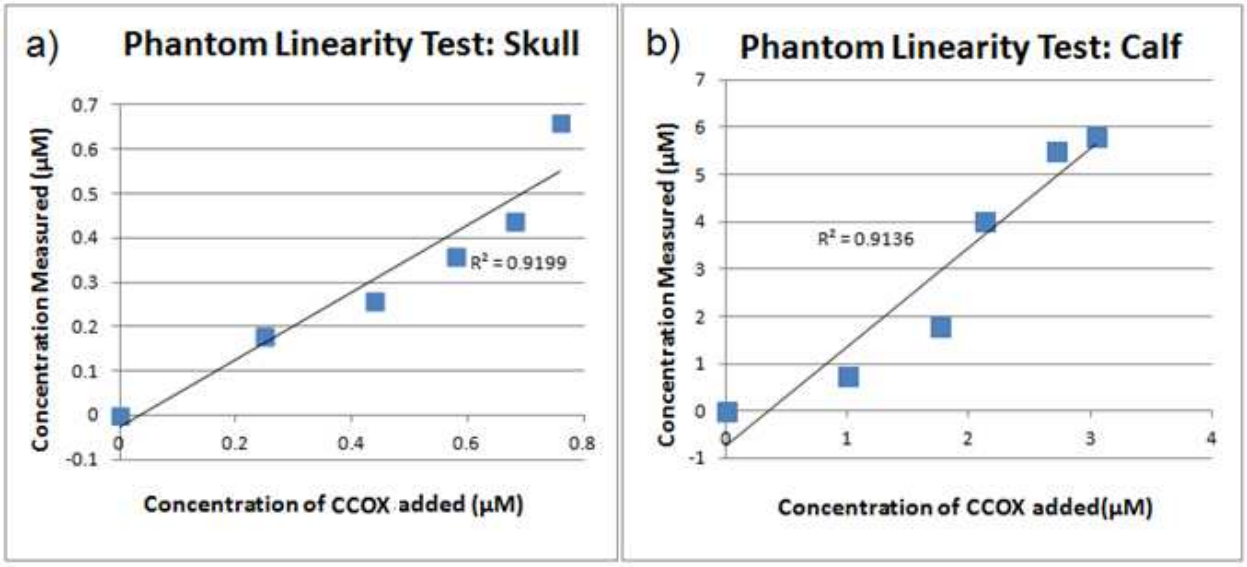

Figure 2.14 Response curves of the system to the phantom experiments performed. The curve for (a) shows response obtained in a phantom mimicking skull optical properties. The curve in (b) shows the response from the phantom mimicking the calf muscles.

After the probe was shown to be able to detect the CCOX in the phantom another experiment was performed to see if the probe could detect the redox state of the CCOX in the same phantom. Since the calf geometry was the most responsive the test was performed using this phantom. An amount of CCOX was added to the phantom. After a brief time, the CCOX was reduced by using the strong reducing agent Sodium Dithionite (Sigma Aldrich). The CCOX was then allowed to oxidize by opening the probe to oxygen. Then a second bolus of Dithionite was added. The results of this experiment can be seen in figure 2.14. The results of the reduction oxidation experiment show that the probe is able to determine the difference between reduced and oxidized CCOX.

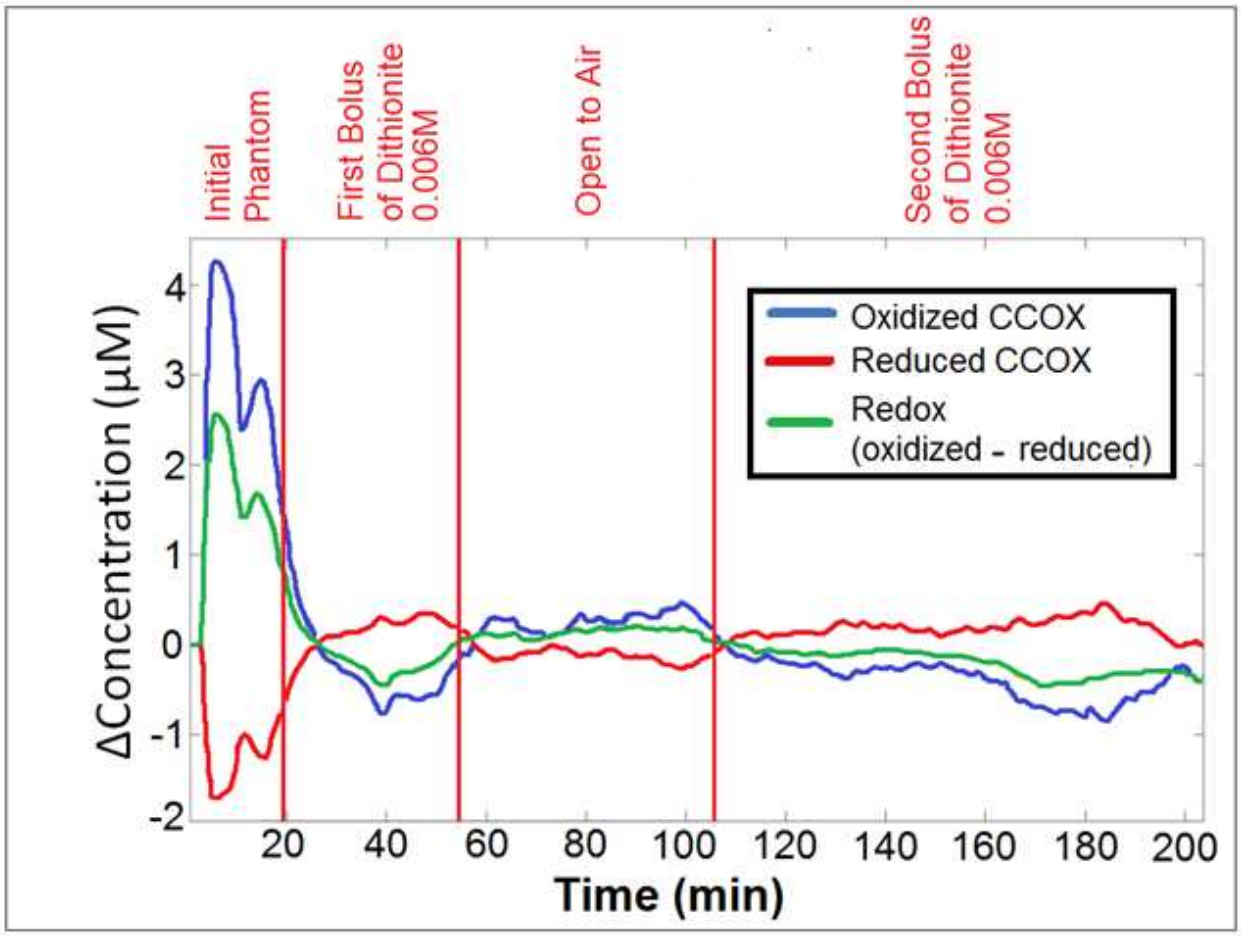

Figure 2.15 The redox state response to adding dithionite and opening the phantom up to oxygen. The oxidation was incomplete because the there is still sodium dithionite in the solution.

Chapter 3: Clinical Data

Clinical Data

In order to obtain clinical data, the cytoximeter device was used in conjunction with an ongoing study at MCW involving patients undergoing a standard of care neurological exam in collaboration with Drs Whelan and Chemlinsky. This decision was made for two reasons; it could be done alongside other instruments used at MCW for verification of our data, and the expected effects of a tilt table on Hb and HbO_2 and CCOX were well understood.

3.1 Experimental Protocol

At the Children's Hospital of Wisconsin, n=14 subjects were monitored while undergoing a standard of care neurological exam. As part of this exam, they were subjected to a heads up tilt table test. During this time, the probe was attached to their gastrocnemius muscle. The experimental setup is shown in figure 3.1. On the other side of their calf a commercially available oximeter was placed. The two devices were run in parallel while the subject underwent a 70° tilt for 60 minutes. This test was designed to exacerbate symptoms that the subjects were experiencing. Because of this condition, n=6 of tests were ended early because the subjects either fainted or were in too much discomfort to continue. As a result, n=8 of the subjects' data were counted in data processing for this experiment.

Ambient light and baseline levels of light were obtained after the application of the probe on the calf muscle but before each of the tilts were performed. After these processes were completed, several minutes of acquisition were performed with the subject in a prone position to make sure that there were no extraneous causes of the signals changing.

The results of the commercial Covidian pulse oximeter were used to verify the measurements made by other cytoximeter probe. The first time the tilt was performed the ambient light was recorded while the Covidian probe was running to determine if the close

placement of the two probes would introduce a cross talk problem. As expected the Covidian probe did not produce an observable noise in the cytoximeter probe.

Figure 3.1 Experimental setup of the tilt table tests. The patient is monitored during a 70 degree tilt. Attached to either side of the gastrocnemius are the (a) Covidian Oximeter that monitors strictly O_2 saturation and (b) the custom built cytoximeter probe that was constructed for this project.

3.1.1 Tilt Table Test

The subjects were secured in the tilt table with their legs restrained. This was done by the clinicians so that the posture of the patient could not change and affect the outcome of the test. They were raised to a posture of 70 degrees of upright. This position was particularly useful in diagnosing issues with orthostatic intolerance as it produces enough stress to cause symptoms in sufferers, but not enough stress to produce many false positives (49).

A natural response to going to an upright position from a prone position is to have an influx of blood reach the lower extremities from the upper body. This leads to venous pooling where blood is not returned to the heart at a rate as fast as it arrives to the legs. In this situation, blood volume increases in the legs and O_2 saturation decreases in the legs. As a way to reduce the

level of venous pooling, there is a change in the tone of the leg muscles where the heart rate increases. Both these responses help return the blood back to the heart. Therefore, we expected to see these signal trends in our oximeter probe data. The levels of deoxyhemoglobin should increase, the levels of oxyhemoglobin should remain relatively stationary and the CCOX redox state should be reduced.

Subjects are kept in the tilted position for 60 minutes. Both the Covidian and custom built cytoximeter recorded data for 5 min before the test and for a 10-minute recovery period after the patient has been lowered from the tilt.

3.2 Data analysis

One of the major problems that has been present in each of the generations of the probe has been removing noise from the raw data during data processing. The problem is particularly challenging in the cytoximeter because of the high degree of collinearity. Collinearity is a measurement of the amount of similarity between explanatory variables in a multivariate regression problem. This problem is very common in spectroscopy analysis since the different species of a single chromophore often differ very little and are only distinguishable in select areas of the spectrum (50, 51). As a regression matrix becomes more collinear, the estimates of the explanatory variables become less and less accurate. This is because as the regression matrix becomes closer to a singular matrix and the inverse matrix becomes larger. The effect is that the noise and uncertainty in the raw measurements become amplified when making estimates of the explanatory variables.

Although precautions were taken to make the best possible regression matrix as described by equation 1.6 in section 1.3.2 there will still always be a certain level of collinearity in the regression matrix. It can be seen from figure 1.2 that there is a similar trend between both species

of hemoglobin and between each species of cytochrome c oxidase. Furthermore, all four chemicals are highly absorbing in the range of 600 nm to 700 nm and comparatively less absorbing in higher wavelengths. This similarity is what is meant by collinearity. A simple test of the amount of collinearity in the regression matrix is the condition number of the matrix. This number can be obtained by using the MATLAB function svd. This function performs the singular value decomposition (SVD) to obtain the singular values of the matrix (52). The SVD decomposes a matrix into an orthonormal input matrix, an orthonormal output matrix, and a set of scaling parameters that relates the two. These scaling parameters are known as singular values denoted by σ. The ratio of the largest and smallest singular value is equal to be the condition number.

Parameter	2 Wavelength Oximetry (735nm, 850nm)	3 Wavelength Oximetry (735nm, 805nm, 850nm)	6 Wavelength Cytoximeter Probe (600nm,620nm,650nm735nm, 805nm, 850nm)
Min σ	0.0426	0.0576	0.0531
Max σ	1.5481	1.6816	4.9947
Condition number	36.3404	29.1944	94.06

Table 3.1 Condition numbers inherent to each of the strategies for oximetry. The smaller the condition number the more suitable it is for measurement.

As can be seen from table 3.1 the condition number has greatly increased when all six wavelengths of the cytoximeter were added. This large condition number means that a new data processing technique should be used to calculate the amounts of Hb, HbO_2 and CCOX species in the subjects. There are several methods used in industry and academia such as principle component analysis (PCA), partial least squares (PLS) and Kalman filtering (53-55). I chose

Kalman filtering for this application because of the fact that PCA and PLS both require high dimensional data sets and would not work with our six source strategy.

3.2.1 Kalman Filtering

I implemented a Kalman filtering algorithm in my Matlab post processing program. Although the algorithm is causal and therefore could be implemented online, when I tried to implement the algorithm in LabVIEW the program's timing was thrown out of sync. Matlab provides several tools for implementing the Kalman filter. A Kalman filter operates by making both a prediction and a measurement at each of the time points during the data acquisition. It combines the prediction and the measurement to find the most likely estimate while taking into account the confidence of the prediction and noise in the measurement.

In order to make a prediction about the concentrations of CCOX, Hemoglobin and Deoxyhemoglobin, their changes must be modeled. Because the cytoximeter samples at discrete points in time, this system will be modeled by a discrete state-space model (55, 56). For this study, each of the absorbing species was assumed to be undergoing a random walk. The equations for a state space model are

$$\begin{aligned} x(k+1) &= A * x(k) + B(k) * u(k) + w(k) \\ y(k) &= C * x(k) + D * u(k) + v(k) \end{aligned} \tag{3.1}$$

the x vector is known as the state vector. It is a four by one vector that represents the amount of each chromophore in the tissue at a given time point k. The matrix A is the state transition matrix, since this model is for a random walk this will be an identity matrix meaning that if there is no input to the system the concentrations will stay the same. The B matrix is the input matrix relating the input to the change in the states, since this is considered to be a random

walk the *B* matrix is an empty matrix and there is no input. The *y* vector is the measurement vector. It is a six by one vector that contains the optical densities of each of the wavelengths. The *C* matrix is the observation matrix relating the states to the observation vector, in this model the *C* matrix is a four by six matrix that contains the absorption coefficients of chemicals at each wavelength. The *D* matrix is the feed forward matrix that adds the input directly to the output vector *y*. Like the *B* matrix, the *D* matrix is also empty because there is no input. The *w* and *v* matrices are the two random noise variables in the model. These random variables are Gaussian and have a covariance defined by w_σ and v_σ matrices. The *w* variable models the random perturbations to the states, this is the factor that will cause the random walk in the states. The *v* matrix models the measurement noise taken.

The Kalman filter is performed in two steps. The first step is to determine a prediction for the states as well as a level of confidence for this prediction. If the model is a zero order random walk model like the one described by equation 3.1, the following equation is used:

$$\begin{aligned} x'(k+1) &= A * x(k) \\ P'(k) &= A * P(k-1) * A^t + w(k) \end{aligned} \tag{3.2}$$

In this step *x'* is the estimate for the values of the state and *P(k)* is the covariance matrix representing the uncertainty in this estimate.

The second step in the Kalman filter is to update this prediction using measurements. This step takes into account both the confidence in the prediction and the noise that is involved in taking these measurements. This equation is as follows:

$$\begin{aligned} K &= P(k) * C^t[v + C * P'(k) * C^t]^{-1} \\ x(k+1) &= x'(k) + K(k) * [y(k) - C * x'(k)] \\ P(k+1) &= P'(k) - K(k) * A * P'(k) \end{aligned} \tag{3.3}$$

These equations are performed on each data point in the recorded data set. Choosing a random walk model simplified this processes the prediction and updating. A random walk model has no the input or feed forward matrices. If a model had either a input or feedforward matrix these steps would have been more complicated.

The selection of covariance matrices w_σ and v_σ greatly affected the appearance of the data after processing. The v_σ matrix was determined by taking the covariance of the light levels while the probe was placed upon a phantom. The w_σ matrix was determined empirically by estimating the rate of change from experiment that did not involve the Kalman filtering procedure. The v_σ matrix used was:

$$v_\sigma = \begin{array}{c|cccccc} & 600nm & 620nm & 650nm & 735nm & 805nm & 850nm \\ 600nm & .3 & .01 & .01 & .01 & .01 & .01 \\ 620nm & .01 & .3 & .01 & .01 & .01 & .01 \\ 650nm & .01 & .01 & .3 & .01 & .01 & .01 \\ 735nm & .01 & .01 & .01 & .3 & .01 & .01 \\ 805nm & .01 & .01 & .01 & .01 & .3 & .01 \\ 850nm & .01 & .01 & .01 & .01 & .01 & .3 \end{array} \quad (3.4)$$

The w_σ matrix that was eventually used was:

$$w_\sigma = \begin{array}{c|cccc} & cyt\ ox & cyt\ red & Hb & HbO_2 \\ cyt\ ox & .04 & -.03 & 0 & 0 \\ cyt\ red & -.03 & .04 & 0 & 0 \\ Hb & 0 & 0 & .4 & -.3 \\ HbO_2 & 0 & 0 & -.3 & .4 \end{array} \quad (3.5)$$

This matrix indicates that the average change in the species of CCOX are one tenth of the change in the hemoglobin species and in general when oxidized CCOX increases the amount reduced CCOX decreases. The same relationship exists between hemoglobin and deoxyhemoglobin. After discarding *B* and *D*, the w_σ and v_σ matrices are added.

The model from equation 3.1 becomes:

$$\begin{matrix} C'_{(cyt\ ox)} \\ C'_{(cyt\ red)} \\ C'_{(cyt\ Hb)} \\ C'_{(cyt\ HbO_2)} \end{matrix} = \begin{matrix} 1 & 0 & 0 & 0 \\ 0 & 1 & 0 & 0 \\ 0 & 0 & 1 & 0 \\ 0 & 0 & 0 & 1 \end{matrix} * \begin{matrix} C_{(cyt\ ox)} \\ C_{(cyt\ red)} \\ C_{(cyt\ Hb)} \\ C_{(cyt\ HbO_2)} \end{matrix} + \mathrm{N}_4(0, w_\sigma)$$

$$\begin{matrix} OD_{600} \\ OD_{620} \\ OD_{650} \\ OD_{735} \\ OD_{805} \\ OD_{850} \end{matrix} = \begin{matrix} & cyt\ ox & cyt\ red & Hb & HbO_2 \\ 600nm & .3 & .01 & .01 & .01 \\ 620nm & .01 & .3 & .01 & .01 \\ 650nm & .01 & .01 & .3 & .01 \\ 735nm & .01 & .01 & .01 & .3 \\ 805nm & .01 & .01 & .01 & .01 \\ 850nm & .01 & .01 & .01 & .01 \end{matrix} * \begin{matrix} C_{(cyt\ ox)} \\ C_{(cyt\ red)} \\ C_{(cyt\ Hb)} \\ C_{(cyt\ HbO_2)} \end{matrix} + \mathrm{N}_6(0, v_\sigma) \quad (3.6)$$

Where $\mathrm{N}_n(\mu, \sigma)$ is a n x 1 random vector drawn from a distribution of covariance σ and mean μ.

The results of this method can be seen in figure 3.2. In this figure, it can be seen that the general trends of the signals have been preserved but the noise is greatly reduced.

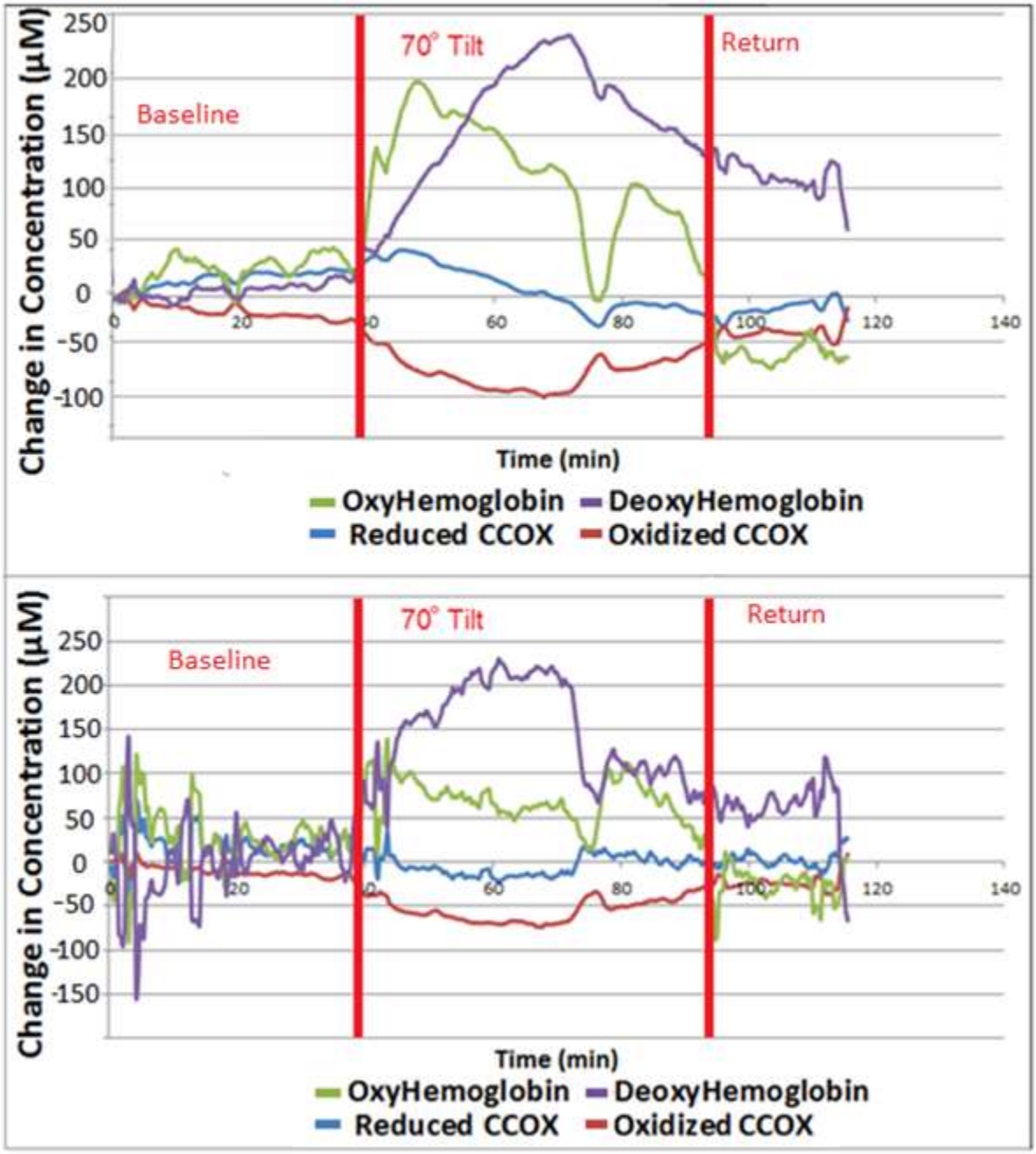

Figure 3.2 Comparison of the data that has been analyzed using the Kalman Filter (top) and using only the Regression equations discussed in chapter 1 (bottom). The trends are generally unaffected by the filtering but the random noise artifacts are largely removed.

3.3 Clinical Data

3.3.1 Standard Subject Response

The cytoximeter probe strongly correlated with the Covidian Oximeter. The Covidian device is a two wavelength oximeter only able to monitor the O_2 saturation levels. Since the device is widely used in clinical settings, it is a good validation device for any custom built oximetry device. The device samples at a rate of one point every six seconds and so is not as fast as even the slowest settings on the cytoximeter. This speed required the cytoximeter be down-sampled to report data on the same time scales as the Covidian probe. These two devices both report O_2 saturation values.

In figure 3.3, it can be seen that the cytoximeter is reporting that the subject's blood volume is increasing while each of the devices report a decrease in O_2 saturation. This matches the expectation that venous pooling would occur during the tilt. During this period deoxygenated blood is collecting in the calf. The extra deoxygenated blood would contribute to a heightened blood volume and decreased O_2 saturation. The CCOX signals both decreased during the tilt, but the CCOX redox state changed towards the more reduced. The signal from the CCOX is likely diluted by the effects of the increased blood volume.

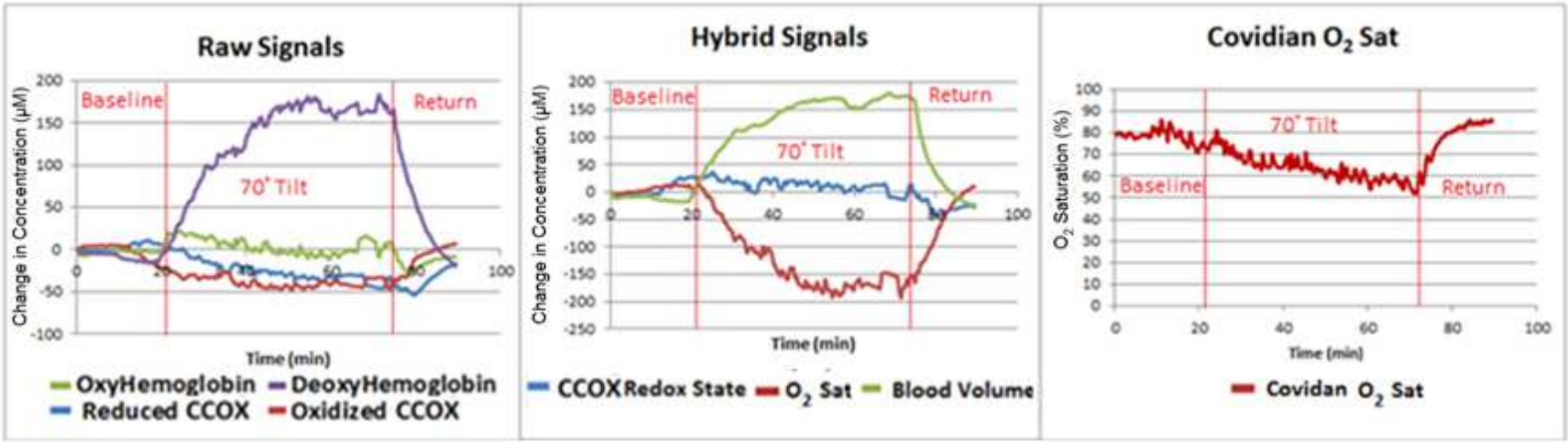

Figure 3.3 Signals collected by the cytoximeter probe and Covidian simultaneously. The estimates of the change in concentration of each signal (left) is obtained by the cytoximeter probe. These are used to generate the hybrid signals (center). The Covidian is used to produce an O_2 saturation signal (right) that can be compared to the O_2 saturation from the cytoximeter probe to show a high level of agreement.

Several of the subjects were unable to continue the procedure for the entire course of the experiment either due to loss of consciousness or because of extreme discomfort. While these experiments were ended prematurely, the data from each of them was still obtained and could be useful in later work for determining the cause of the fainting. A full analysis of this group of patients is outside the scope of this thesis; however, initial data analysis can be seen for one patient in figure 3.4.

The majority of the subjects who were able to finish the procedure exhibited an increase in both oxyhemoglobin and deoxyhemoglobin during the tilt. Subjects that were unable to finish showed a decrease in oxyhemoglobin levels as the tilt began. Additionally, they exhibited a much slower recovery than subjects who did finish the tilt.

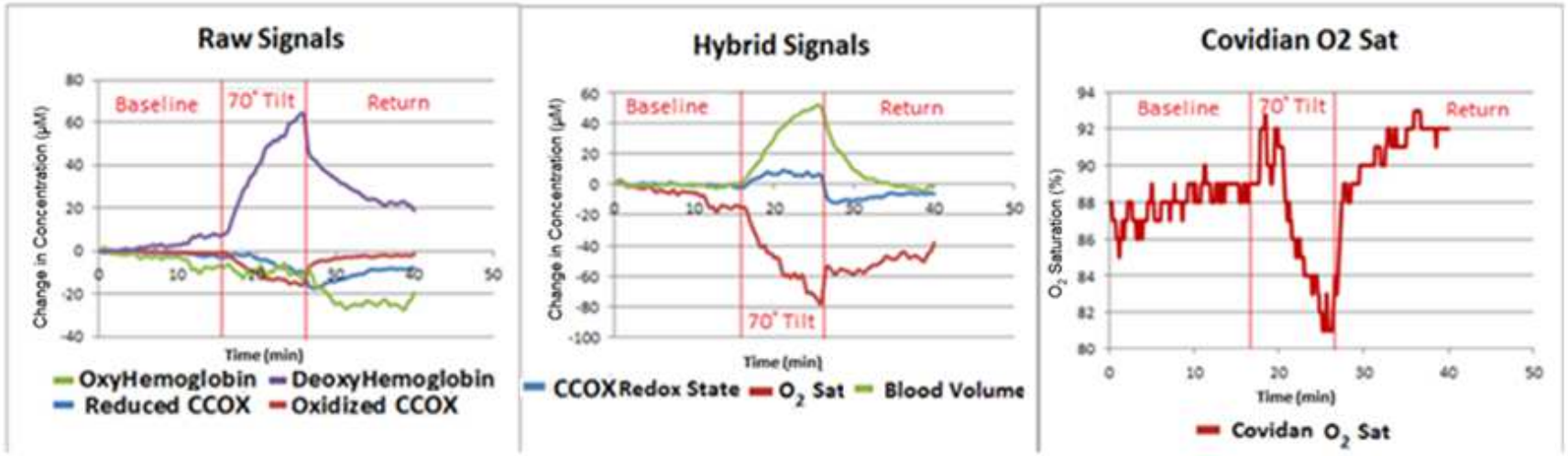

Figure 3.4 Data from a subject who fainted during the experimental protocol. Unlike subjects who could finish the tilt table test HbO_2 levels drop as the tilt began. It is also important to note that the drop in O_2 saturation occurs faster than in the other subjects.

3.3.2 Statistical Analysis

Because the subjects that fainted would often do so because of an inability to regulate their blood volume and O_2 saturation their data is excluded from this section of the discussion. The remaining 8 data sets were normalized so that the tilts would be located in the same time and could be averaged together these results are reported on the next page both as an average response and as a statistical breakdown of responses. Of the 8 subjects that could be utilized in this section 7 (84%) of them presented with a more reduced CCOX redox state. This suggests that the device is recorded an increase in muscle tone in these subjects. Furthermore, the fact that the change in concentrations in all these subjects are consistent is highly suggestive that the device was reliable in its assessment of in-vivo CCOX readings.

Because the concentration of hemoglobin were much larger than CCOX, to provide an easy visualization of the results obtained by the cytoximeter the signals are separated into a number of figures. The CCOX measurements are presented in figure 3.5. This figure contains the data for the concentrations of reduced CCOX, oxidized CCOX and the redox state of the CCOX. Figure 3.6 contains the hemodynamic responses. This is the concentrations of hemoglobin, deoxyhemoglobin, blood volume, and O_2 saturation. To show that the variability in these measurements was similar to those obtained by the Covidian oximeter, a summary of the Covidian's responses is also included in figure 3.7. Lastly a side by side comparison of the tilts obtained in this study is shown in figure 3.8.

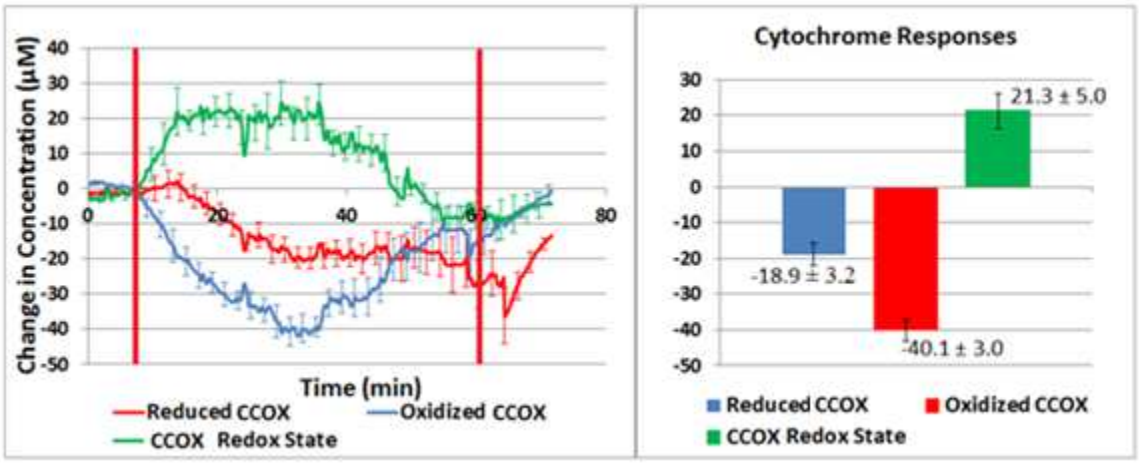

Figure 3.5 Average CCOX responses in subjects who were able to complete each of the Tilt Table Tests. The concentration of the two absorbing molecules, oxidized and reduced CCOX, are presented as well as the redox state. These signals are reported with the standard error of each signal plotted around the signal. The maximum level of each signal was recorded and the average of the maximums is reported on the right.

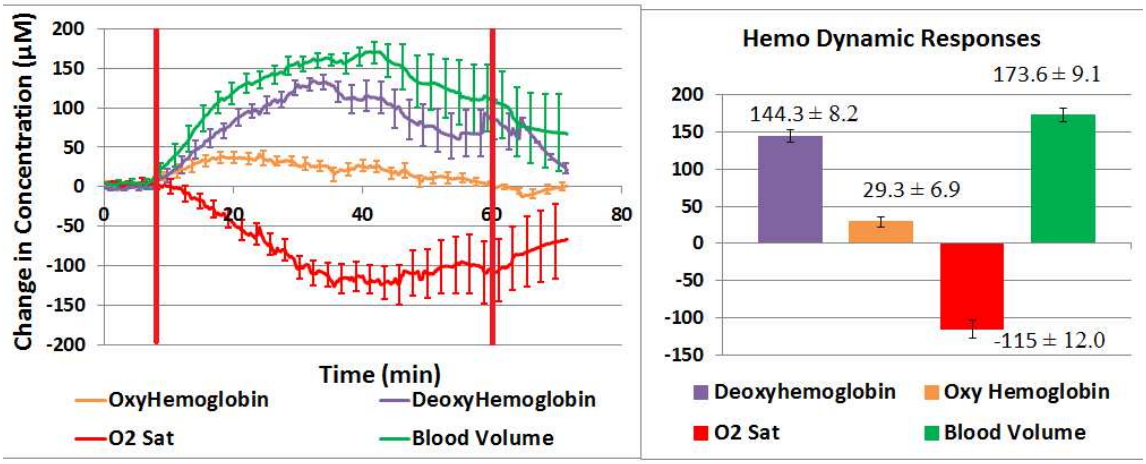

Figure 3.6 Average Hemodynamic responses in subjects who were able to complete each of the Tilt Table Tests. The two single chromophores oxyhemoglobin and deoxyhemoglobin are reported. Also reported are the O_2 saturation and blood volume signals. All four of these signals are reported with the standard error of each signal plotted around the signal. The maximum level of each signal were recorded and the average maximum response is reported on the right.

To show that the variability in these measurements was similar to those obtained by the Covidian oximeter, a summary of the Covidian's responses is also included in figure 3.7. Lastly a side by side comparison of the tilts obtained in this study is shown in figure 3.8.

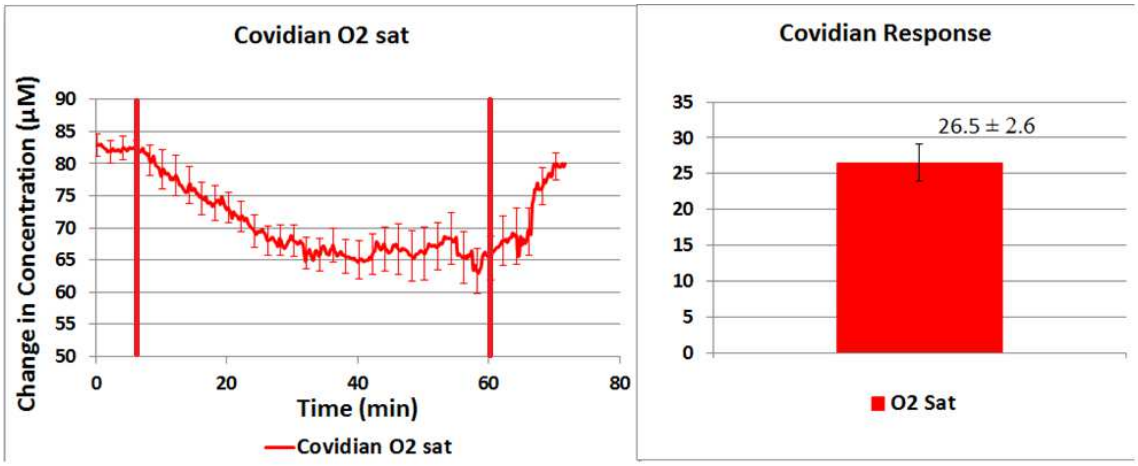

Figure 3.7 Average Cytochrome O_2 saturation as recorded by the Covidian. The Covidian signal is reported with standard error over the 8 experiments. The maximum decrease in O_2 saturation in each of the 8 subjects were averaged. The average of maximum O_2

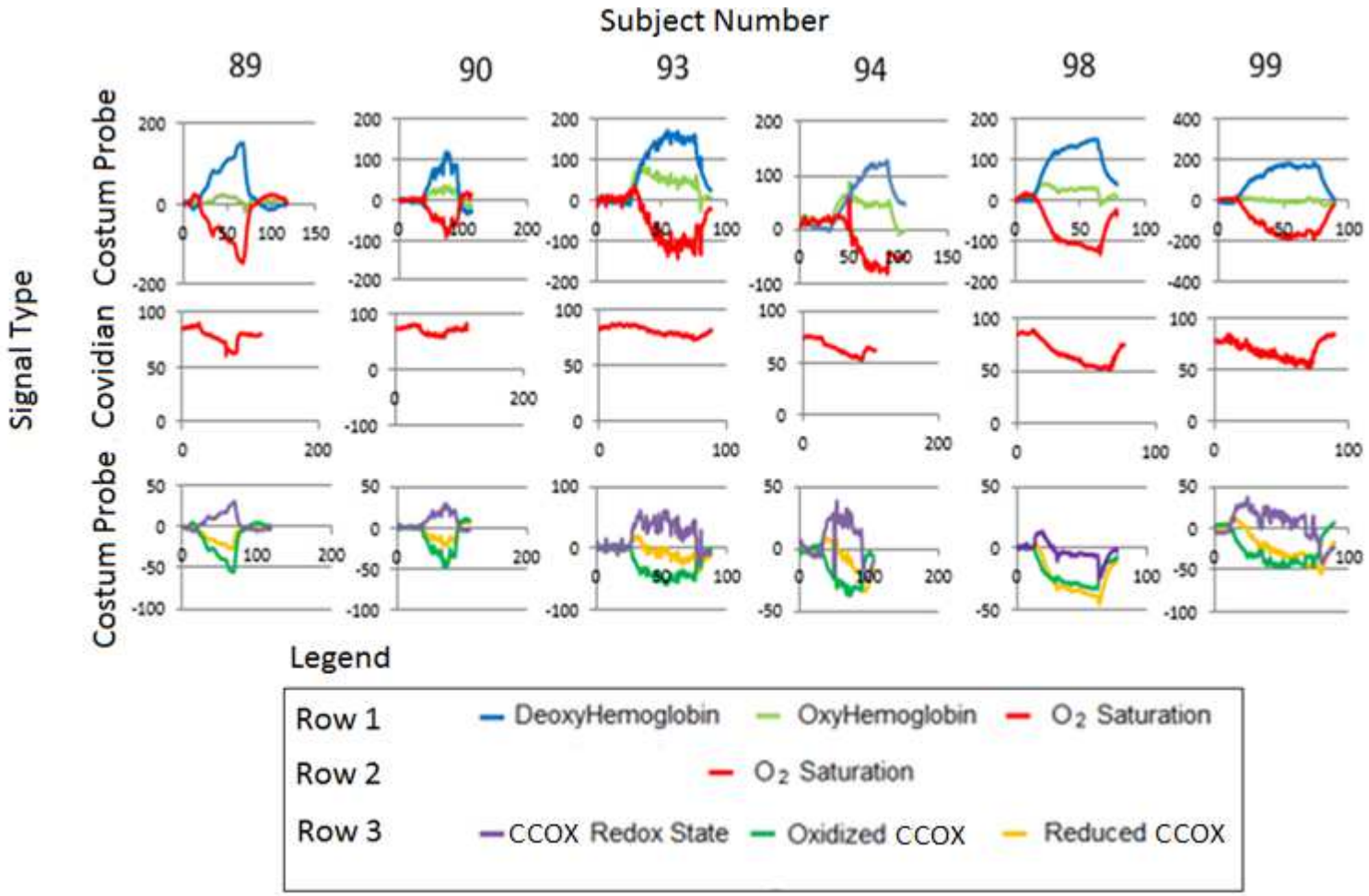

Figure 3.8 side by side comparison of six of the subject's data used to generate the figures in this section.

3.4 Force Correlation

In order to show that the CCOX redox state changes with muscular effort, two additional experiments have been conducted. The first experiment aimed to measure CCOX redox state in forearm as the subject squeezed a force grip. The second aimed to measure CCOX redox state in the calves as the subject performed calf raises. The results of some representative results are discussed in this section.

3.4.1 Forearm Muscle Experiment

The probe was attached to the flexor digitorum muscle of the subject. The subject would squeeze the force grip, thus exercising their flexor digitorum muscles. The experimenter recorded the periods of time during which the subject was squeezing. The results of the cytoximeter data one of these experiments are seen in figure 3.9.

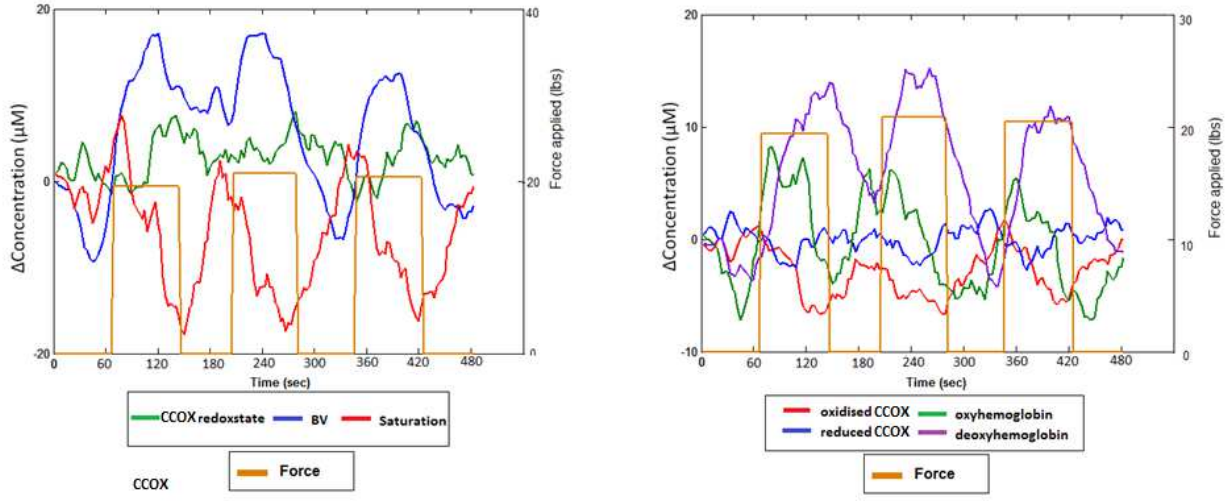

Figure 3.9 The results from a force grip experiment. As the subject squeezes the force grip with their hand, their forearm muscles are undergoing metabolic activity. The O_2 saturation decreases as oxygen is consumed. The CCOX Redox state becomes more reduced during this time because of the metabolic activity.

3.4.2 Calf Muscle Experiment

The Probe was attached to the gastrocnemius of the subject. The subject then stood on their toes lifting their heels off the ground to exercise their calf muscles. The experimenter made comments in the program indicating the times at which the r lifted their heels. The results of a representative of these experiments are shown in figure 3.10.

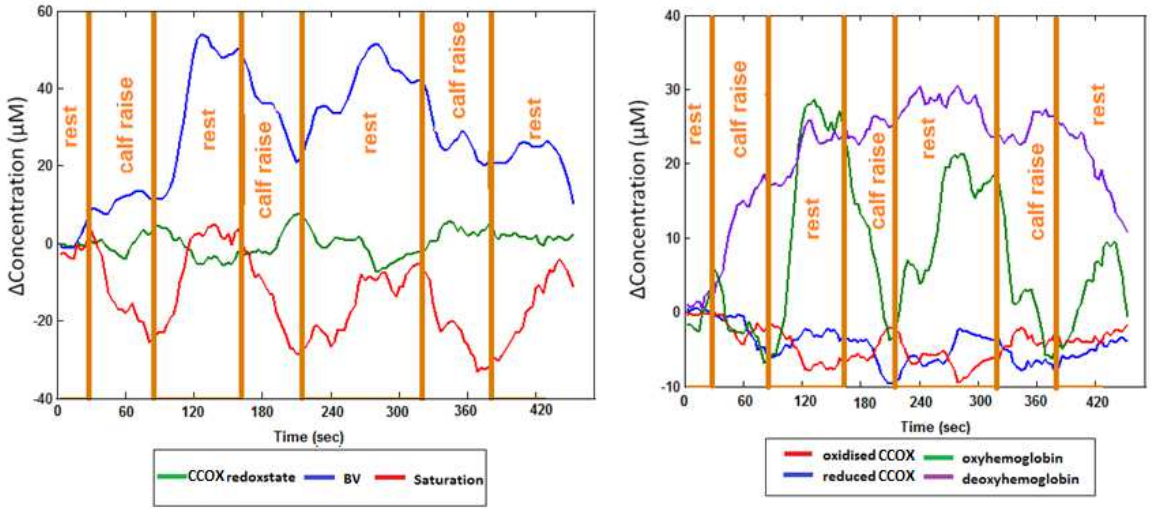

Figure 3.10 The results of a calf exercise experiment. It can be seen that the O_2 saturation decreases as the calf muscle is exercised. There is also a shift towards more reduced in the redox state of the CCOX as the muscle is exercised.

3.4 Conclusions and Discussion

The purpose of the collected data from these experimental protocols was to detect changes in CCOX and hemodynamic signals. The fact that the CCOX signals are largely independent of the blood volume and assume different rates of changes and signal shapes is important because it means that these signals are not likely to be caused by an artifact from the increasing amounts of blood. These results are promising and could be used to assess the health of patients suffering from POTS, by monitoring the health of their calf muscles.

The tilt table tests demonstrated that the subjects are experiencing venous pooling during the tilt. The CCOX redox state observed during the tilt suggests that the subject's muscle tone in their legs is increasing to combat the effects of the venous pooling.

Two experiments targeting two different muscle groups have demonstrated that the CCOX redox state changes when those muscles are exercised. The work continues to correlate the amount of muscular exertion to the CCOX redox state. When this research is completed with a larger number of patients, we will have a direct quantitative parameter of tissue metabolism and oxygenation of tissue in patients.

Chapter 4: Conclusion and Future Work

4.1 Conclusion

I have designed a device known as the cytoximeter, which uses six wavelengths to non-invasively monitor levels of CCOX and perform oximetry simultaneously. This device was specifically designed to monitor metabolic function in superficial tissues. Knowledge of tissue optics was used to choose the wavelengths of the device. After performing numerical simulations of photon migration, the source detector separations were chosen to target superficial tissues.

In the course of designing the cytoximeter, I have also implemented several phantom validations. The cytoximeter has demonstrated the ability to monitor the concentration of CCOX in tissue mimicking phantoms. The device was also shown to be sensitive to the redox state of CCOX in these phantoms.

The probe was then applied to study the function of calf muscles in patients suffering from POTS. It showed that these patients are likely experiencing venous pooling. The results also suggest that their bodies are increasing the muscle tone in their calves to try and increase the rate that blood returns to the heart. The hemodynamic changes recorded by the cytoximeter were highly correlated with the data collected from a commercially available oximeter.

Lastly, the work in progress correlates the changes in CCOX redox in a muscle to the amount of force generated by that muscle. Once this work is completed, the device will have the ability to quantitatively assess the levels of metabolic activity in biological tissues.

A device with these abilities would have many applications in clinical settings. These could include monitoring the activation of brain tissue during an event such as an epileptic seizure. Or monitoring the recovery of stroke affected muscles by monitoring the metabolic activity in those muscles.

4.2 Future Work

The problem of inter patient variability is a consistent problem in NIRS. Variations in skin pigment and arm composition can cause many signal processing challenges. Independent component analysis (ICA) has been used to remove the effects of skin pigmentation on NIRS measurements (57).

The signal at each of the detectors would be partially due to signals generated by both shallow and deeper layers of tissue. Each detector therefore would be receiving a mixed signal without any knowledge of how these signals are mixed. ICA could be used to separate the signals that are caused by the shallower and deeper tissues (58).

The ICA algorithm will be necessary to obtain signals from the brain, which is the next goal of this project. The algorithm needs to be employed to remove the effects of the blood in the scalp so that the signal from the brain can be isolated.

One of the most persistent challenges in this research was the durability of the probe. Several Ideas for creating a more robust and reliable probe have been advanced and have begun to be developed. The first major improvement is that the group has decided to pursue creating a 3D printed probe. This will allow the probe to be much more durable and compact. Also a flexible PCB could be incorporated into the design of the probe to minimize the chances of the components in the probe losing electrical contact. A more robust and artistic probe design is one of the major opportunities for future students to focus on.

Bibliography

1. Taillefer MC, Denault AY. Cerebral near-infrared spectroscopy in adult heart surgery: systematic review of its clinical efficacy. Can J Anaesth. 2005;52(1):79-87.

2. Trapp EG, Chisholm DJ, Boutcher SH. Metabolic response of trained and untrained women during high-intensity intermittent cycle exercise. Am J Physiol Regul Integr Comp Physiol. 2007;293(6):R2370-5.

3. Ferrari M, Binzoni T, Quaresima V. Oxidative metabolism in muscle. Philos Trans R Soc Lond B Biol Sci. 1997;352(1354):677-83. PMCID: 1691965.

4. Faber DJ, Aalders MC, Mik EG, Hooper BA, van Gemert MJ, van Leeuwen TG. Oxygen saturation-dependent absorption and scattering of blood. Phys Rev Lett. 2004;93(2):028102.

5. Boushel R, Langberg H, Olesen J, Gonzales-Alonzo J, Bulow J, Kjaer M. Monitoring tissue oxygen availability with near infrared spectroscopy (NIRS) in health and disease. Scand J Med Sci Sports. 2001;11(4):213-22.

6. Lin YQ, Lech G, Nioka S, Intes X, Chance B. Noninvasive, low-noise, fast imaging of blood volume and deoxygenation changes in muscles using light-emitting diode continuous-wave imager. Rev Sci Instrum. 2002;73(8):3065-74.

7. Wolf U, Wolf M, Choi JH, Levi M, Choudhury D, Hull S, et al. Localized irregularities in hemoglobin flow and oxygenation in calf muscle in patients with peripheral vascular disease detected with near-infrared spectrophotometry. J Vasc Surg. 2003;37(5):1017-26.

8. Wolf M, Ferrari M, Quaresima V. Progress of near-infrared spectroscopy and topography for brain and muscle clinical applications. J Biomed Opt. 2007;12(6):062104.

9. Chance B, Dait MT, Zhang C, Hamaoka T, Hagerman F. Recovery from exercise-induced desaturation in the quadriceps muscles of elite competitive rowers. Am J Physiol. 1992;262(3 Pt 1):C766-75.

10. Gaitanos GC, Williams C, Boobis LH, Brooks S. Human muscle metabolism during intermittent maximal exercise. J Appl Physiol (1985). 1993;75(2):712-9.

11. Cooper CE, Matcher SJ, Wyatt JS, Cope M, Brown GC, Nemoto EM, et al. Near-infrared spectroscopy of the brain: relevance to cytochrome oxidase bioenergetics. Biochem Soc Trans. 1994;22(4):974-80.

12. Michel H, Behr J, Harrenga A, Kannt A. Cytochrome c oxidase: structure and spectroscopy. Annu Rev Biophys Biomol Struct. 1998;27:329-56.

13. Abed H, Ball PA, Wang LX. Diagnosis and management of postural orthostatic tachycardia syndrome: A brief review. J Geriatr Cardiol. 2012;9(1):61-7. PMCID: 3390096.

14. Raj SR. Postural tachycardia syndrome (POTS). Circulation. 2013;127(23):2336-42.

15. R RS. The postural tachycardia syndrome (POTS): pahtopysiology, diagnosis & management. indian pacing and electrophysiology journal. 2006;6(2):84.

16. Hoad A, Spickett G, Elliott J, Newton J. Postural orthostatic tachycardia syndrome is an under-recognized condition in chronic fatigue syndrome. Qjm-Int J Med. 2008;101(12):961-5.

17. Joyner MJ, Masuki S. POTS versus deconditioning: the same or different? Clin Auton Res. 2008;18(6):300-7. PMCID: 3770293.

18. Dahan S, Tomljenovic L, Shoenfeld Y. Postural Orthostatic Tachycardia Syndrome (POTS) - A novel member of the autoimmune family. Lupus. 2016;25(4):339-42.

19. Stewart JM. Autonomic nervous system dysfunction in adolescents with postural orthostatic tachycardia syndrome and chronic fatigue syndrome is characterized by attenuated vagal baroreflex and potentiated sympathetic vasomotion. Pediatr Res. 2000;48(2):218-26.

20. Kuz'mich VV, Zharov VP. [Basic principles and characteristics of transcutaneous "reflective" oximetry]. Med Tekh. 1993(3):36-42.

21. Haynes JM. The ear as an alternative site for a pulse oximeter finger clip sensor. Respir Care. 2007;52(6):727-9.

22. Rafeal Ortega CJH, Kelly Elterman, Albert Woo. Pulse oximetry. New England Journal of Medicine. 2011;364(16):33.

23. Yodh A, Chance B. Spectroscopy and Imaging with Diffusing Light. Phys Today. 1995;48(3):34-40.

24. Maikala RV. Modified Beer's Law - historical perspectives and relevance in near-infrared monitoring of optical properties of human tissue. Int J Ind Ergonom. 2010;40(2):125-34.
25. Tremper KK. Pulse oximetry. Chest. 1989;95(4):713-5.

26. Schnettler JM, Wallace JA. Pulse Oximetry as a Diagnostic-Tool of Pulpal Vitality. J Endodont. 1991;17(10):488-90.

27. Vanneste WH. The stoichiometry and absorption spectra of components a and a-3 in cytochrome c oxidase. Biochemistry. 1966;5(3):838-48.

28. Cooper CE, Springett R. Measurement of cytochrome oxidase and mitochondrial energetics by near-infrared spectroscopy. Philos Trans R Soc Lond B Biol Sci. 1997;352(1354):669-76. PMCID: 1691958.

29. Nelson LA, McCann JC, Loepke AW, Wu J, Ben Dor B, Kurth CD. Development and validation of a multiwavelength spatial domain near-infrared oximeter to detect cerebral hypoxia-ischemia. J Biomed Opt. 2006;11(6):064022.
30. Gagnon RE, Gagnon FA, Macnab AJ. Comparison of 13 published cytochrome c oxidase near-infrared spectroscopy algorithms. Eur J Appl Physiol Occup Physiol. 1996;74(6):487-95.

31. Tuchin V. Light-Tissue Interaction. Vo-Dihn IT, editor. New York: CRC Press; 2003.

32. Tuchin V, tuchin VV. Tissue optics: light scattering methods and instruments for medical diagnosis. Bellingham: SPIE press; 2007.

33. O'Leary M. Imaging with diffuse Photon Density Waves; 1996.

34. Bashkatov AN, Genina EA, Kochubey VI, Tuchin VV. Optical properties of human skin, subcutaneous and mucous tissues in the wavelength range from 400 to 2000 nm. J Phys D Appl Phys. 2005;38(15):2543-55.

35. Firbank M, Hiraoka M, Essenpreis M, Delpy DT. Measurement of the optical properties of the skull in the wavelength range 650-950 nm. Phys Med Biol. 1993;38(4):503-10.

36. Yu G, Durduran T, Lech G, Zhou C, Chance B, Mohler ER, 3rd, et al. Time-dependent blood flow and oxygenation in human skeletal muscles measured with noninvasive near-infrared diffuse optical spectroscopies. J Biomed Opt. 2005;10(2):024027.

37. Wang L, Jacques SL, Zheng L. MCML--Monte Carlo modeling of light transport in multi-layered tissues. Comput Methods Programs Biomed. 1995;47(2):131-46.

38. Boas DA, Culver JP, Stott JJ, Dunn AK. Three dimensional Monte Carlo code for photon migration through complex heterogeneous media including the adult human head. Optics Express. 2002;10(3):159-70.

39. Fang Q, Boas DA. Monte Carlo simulation of photon migration in 3D turbid media accelerated by graphics processing units. Opt Express. 2009;17(22):20178-90. PMCID: 2863034.

40. Zonios G, Dimou A. Modeling diffuse reflectance from homogeneous semi-infinite turbid media for biological tissue applications: a Monte Carlo study. Biomed Opt Express. 2011;2(12):3284-94. PMCID: 3233248.

41. Monte Carlo for multi-layered media. [cited 10 october 2015]; Available from: http://omlc.ogi.edu/software/mc/.

42. Heiskala J, Neuvonen T, Grant PE, Nissila I. Significance of tissue anisotropy in optical tomography of the infant brain. Appl Opt. 2007;46(10):1633-40.

43. Zhao H, Tanikawa Y, Gao F, Onodera Y, Sassaroli A, Tanaka K, et al. Maps of optical differential pathlength factor of human adult forehead, somatosensory motor and occipital regions at multi-wavelengths in NIR. Phys Med Biol. 2002;47(12):2075-93.

44. Advanced Mechanical Technology I. MC3A-1000 datasheed. [cited 8-april-2014]; Available from: http://www.amti.biz/

45. Cubeddu R, Pifferi A, Taroni P, Torricelli A, Valentini G. A solid tissue phantom for photon migration studies. Phys Med Biol. 1997;42(10):1971-9.

46. Di Ninni P, Martelli F, Zaccanti G. Effect of dependent scattering on the optical properties of Intralipid tissue phantoms. Biomed Opt Express. 2011;2(8):2265-78. PMCID: 3149524.

47. Di Ninni P, Martelli F, Zaccanti G. The use of India Ink in tissue-simulating phantoms. Opt Express. 2010;18(26):26854-65.

48. Madsen SJ, Patterson MS, Wilson BC. The use of India Ink as an optical absorber in tissue-simulating phantoms. Phys Med Biol. 1992;37(4):985-93.

49. Kenny RA, O'Shea D, Parry SW. The Newcastle protocols for head-up tilt table testing in the diagnosis of vasovagal syncope, carotid sinus hypersensitivity, and related disorders. Heart. 2000;83(5):564-9. PMCID: 1760829.

50. Kuo BJ, Su KC, Hong MC, Thseng FS. Prediction of the quality trait in rice (Oryza sativa L.) by near-infrared spectroscopy using different statistical methods. Breeding Sci. 2002;52(1):65-70.

51. Arimoto H, Furukawa H. Retinal Oximetry with 510-600 nm Light Based on Partial Least-Squares Regression Technique. Jpn J Appl Phys. 2010;49(11).

52. Singular Value Cecomposition. [cited]; Available from: http://www.mathworks.com/help/matlab/ref/svd.html.

53. Killner MHM, Rohwedder JJR, Pasquini C. A PLS regression model using NIR spectroscopy for on-line monitoring of the biodiesel production reaction. Fuel. 2011;90(11):3268-73.

54. Balabin RM, Smirnov SV. Variable selection in near-infrared spectroscopy: benchmarking of feature selection methods on biodiesel data. Anal Chim Acta. 2011;692(1-2):63-72.

55. Izzetoglu M, Chitrapu P, Bunce S, Onaral B. Motion artifact cancellation in NIR spectroscopy using discrete Kalman filtering. Biomed Eng Online. 2010;9:16. PMCID: 2846950
.
56. Hu XS, Hong KS, Ge SS, Jeong MY. Kalman estimator- and general linear model-based on-line brain activation mapping by near-infrared spectroscopy. Biomed Eng Online. 2010;9:82. PMCID: 3020171.

57. Kohno S, Miyai I, Seiyama A, Oda I, Ishikawa A, Tsuneishi S, et al. Removal of the skin blood flow artifact in functional near-infrared spectroscopic imaging data through independent component analysis. J Biomed Opt. 2007;12(6):062111.

58. Funane T, Atsumori H, Katura T, Obata AN, Sato H, Tanikawa Y, et al. Quantitative evaluation of deep and shallow tissue layers' contribution to fNIRS signal using multi-distance optodes and independent component analysis. Neuroimage. 2014;85 Pt 1:150-65.